



1 **Climatological distribution of dissolved inorganic nutrients**
2 **in the Western Mediterranean Sea (1981-2017)**

3

4 **Malek Belgacem**^{1,2}, **Katrin Schroeder**¹, **Alexander Barth**³, **Charles Troupin**³, **Bruno**
5 **Pavoni**², **Jacopo Chiggiato**¹

6 ¹CNR-ISMAR, Arsenale Tesa 104, Castello 2737/F, 30122 Venezia, Italy

7 ²Dipartimento di Scienze Ambientali Informatica e Statistica, DAIS, Università Ca' Foscari
8 Venezia, Campus Scientifico Mestre, Italy

9 ³GeoHydrodynamics and Environment Research, GHER, University of Liège, Quartier Agora,
10 Allée du 6-Août, 17, Sart Tilman, 4000 Liège 1, Belgium

11 Correspondence: Malek Belgacem (malek.belgacem@ve.ismar.cnr.it)

12

13

14 **Abstract**

15 The Western MEDiterranean Sea BioGeochemical Climatology (BGC-WMED) presented here is a
16 product derived from in situ observations. Annual mean gridded nutrient fields for the period 1981-
17 2017, and its sub-periods 1981-2004 and 2005-2017, on a horizontal $1/4^\circ \times 1/4^\circ$ grid have been
18 produced. The biogeochemical climatology is built on 19 depth levels and for the dissolved inorganic
19 nutrients nitrate, phosphate and orthosilicate. To generate smooth and homogeneous interpolated fields,
20 the method of the Variational Inverse Model (VIM) was applied. A sensitivity analysis was carried out
21 to assess the comparability of the data product with the observational data. The BGC-WMED has then
22 been compared to other available data products, i.e. the medBFM biogeochemical reanalysis of the
23 Mediterranean Sea and the World Ocean Atlas18 (WOA18) (its biogeochemical part). The BGC-
24 WMED product supports the understanding of inorganic nutrient variability in the western
25 Mediterranean Sea, in space and in time, but can also be used to validate numerical simulations making
26 it a reference data product.

27 **Keywords:** western Mediterranean Sea, climatology, inorganic nutrients, in situ observations.

28 **1 Introduction**

29 Ocean life relies on the loads of marine macro-nutrients (nitrate, phosphate and orthosilicate) and other
30 micro-nutrients within the euphotic layer. They fuel phytoplankton growth, maintaining thus the
31 equilibrium of the food web. These nutrients may reach deeper levels through vertical mixing/upwelling,

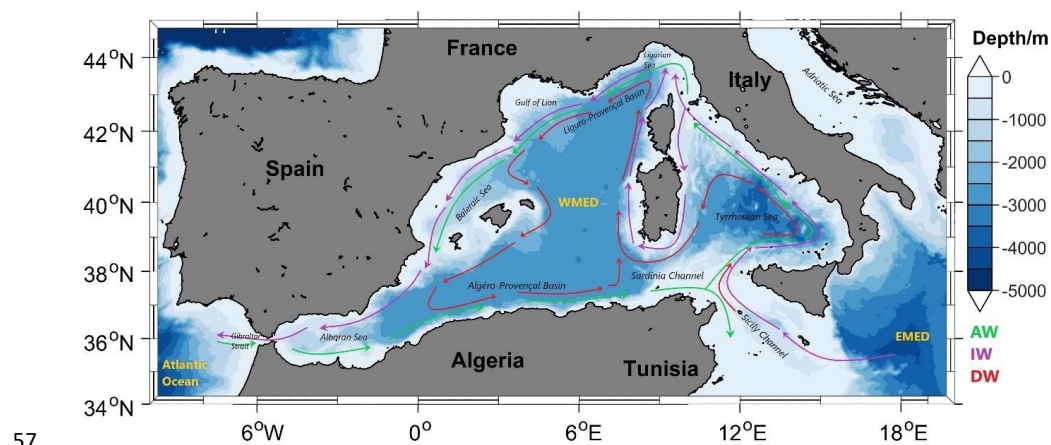


32 and remineralization of sinking organic matter. Ocean circulation and physical processes continually
33 drive the large-scale distribution of chemicals (Williams and Follows, 2003) toward a homogeneous
34 distribution. Therefore, nutrient dynamics is important to understand the overall ecosystem productivity
35 and carbon cycles. In general, the surface layer is depleted in nutrients in low latitude regions (Sarmiento
36 and Toggweiler, 1984), but in some ocean regions, called high nutrient low chlorophyll (HNLC) regions,
37 nutrient concentrations tend to be anomalously high, particularly in areas of the North Atlantic and
38 Southern Ocean, as well as in the eastern equatorial Pacific, and in the North Pacific; see e.g. Pondaven
39 et al. (1999). In the Mediterranean, the surface layer is usually nutrient-depleted. Most studies show that
40 nitrate is the most common limiting factor for primary production in the global ocean (Moore et al.,
41 2013), while others evidence that phosphate may be a limiting factor in some specific areas, as is the
42 case of the Mediterranean Sea (Diaz et al., 2001; Krom et al., 2004).

43 Being an enclosed marginal sea, the Mediterranean Sea exhibits an anti-estuarine circulation,
44 responsible for its oligotrophic character (Bethoux et al., 1992; Krom et al., 2010) and acting like a
45 subtropical anticyclonic gyre. The Atlantic Water (AW), characterized by low-salinity and low-nutrient
46 content, enters the Western Mediterranean Sea (WMED) at the surface, through the Strait of Gibraltar,
47 and moves toward the Eastern Mediterranean Sea (EMED), crossing the Sicily Channel (Fig. 1). In the
48 Levantine and in the Cretan Sea, the AW becomes saltier, warmer and denser, and it sinks to
49 intermediate levels (200-500 m) to form the Intermediate Water (IW, Schroeder et al., 2017). The IW
50 (which may be further called Levantine or Cretan Intermediate Water, LIW or CIW) flows westward
51 across the entire Mediterranean Sea to the Atlantic Ocean (Fig. 1). As for the deep layer, the Western
52 Mediterranean Deep Water (WMDW or DW) is formed in the Gulf of Lion through deep convection
53 (Testor et al., 2018) while the Eastern Mediterranean Deep Water (EMDW) is formed in the Adriatic
54 Sea and occasionally in the Aegean Sea (Lascaratos et al., 1999; Roether et al., 1996, 2007).

55

56



57

58 **Figure 1.** Map of the western Mediterranean Sea showing the main regions with a sketch of the AW,
59 IW and DW major paths.

60 The Mediterranean Sea is known to be a hotspot for climate change (Giorgi, 2006). During the early
61 1990s, the Deep Water (DW) formation area of the EMED shifted from the Adriatic Sea to the Aegean
62 Sea. This event is known as the Eastern Mediterranean Transient (EMT; Roether et al., 1996, 2007,
63 2014; Roether and Schlitzer, 1991; Theocharis et al., 2002). As a consequence, the intermediate and
64 deep waters of the EMED became saltier and warmer (Lascaratos et al., 1999; Malanotte-Rizzoli et al.,
65 1999). The EMT affected the WMED as well, not only changing the thermohaline characteristics of the
66 IW and concurring to the preconditioning of the Western Mediterranean Transition (WMT; Schroeder
67 et al., 2016), which set the beginning of a rapid warming and salting of the deep layers in the WMED
68 since 2005 (Schroeder et al., 2006; Schroeder et al., 2010, 2016; Piñeiro et al., 2019). Over the last
69 decade, it has been evidenced that heat and salt content have been increasing in all over the deep western
70 basin (Schroeder et al., 2016).

71 Changes in circulation due to an increased stratification limit the exchange of materials between the
72 nutrient-rich deep layers and the surface layers. Understanding the peculiar oligotrophy of the
73 Mediterranean Sea is still a challenge, since there is not an exact quantification of nutrient sinks and
74 sources. Studies like Crispi et al. (2001), Ribera d'Alcalà (2003), Krom et al. (2010) and Lazzari et al.
75 (2012) related the horizontal spatial patterns in nutrient concentrations mainly to the anti-estuarine
76 circulation which exports nutrients to the Atlantic Ocean, showing a decreasing tendency of nutrient
77 concentrations toward east, as opposed to the salinity horizontal gradient. These variations, together
78 with the anthropogenic perturbations affect the spatial distribution of nutrients (Moon et al., 2016) while
79 temporal variability is still unresolved.

80 De Fommervault et al. (2015) reported a decreasing phosphate and an increasing nitrate concentrations
81 trend between 1990 and 2010, based on a time series (DYFAMED) in the Ligurian Sea, while Moon et



82 al. (2016) evidenced an increase between 1990 and 2005 and a gradual decline after 2005 in both nitrate
83 and phosphate in the WMED and EMED.

84 At the global scale, most of the biogeochemical descriptions are based on model simulations and satellite
85 observations (using sea surface chlorophyll concentrations (Salgado-Hernanz et al., 2019) but also on
86 the increasing use of Biogeochemical Argo floats (D’Ortenzio et al., 2020; Lavigne, 2015; Testor et al.,
87 2018), since in situ observations of nutrients are generally infrequent and scattered in space and time.
88 For this reason, climatological mapping is often applied to sparse in situ data in order to understand the
89 biogeochemical state of the ocean representing monthly, seasonally, or annually averaged fields.

90 Levitus (1982) was the first to generate objectively analyzed fields of potential temperature, salinity,
91 and dissolved oxygen, and to produce a climatological atlas of the world ocean.

92 Later on the World Ocean Atlas (WOA), the North Sea climatologies and the Global ocean Carbon
93 Climatology resulting from GLODAP data product (Key et al., 2004) used the Cressman analysis (1956)
94 with modified Barnes scheme (Barnes 1964, 1994). In 1994, the first World Ocean Atlas (WOA94;
95 Conkright et al., 1994) was released integrating temperature, salinity, oxygen, phosphate, nitrate, and
96 silicate observations. Every four years there is a renewed release of the WOA with an updated World
97 Ocean database (WOD).

98 On the regional scale, the first salinity and temperature climatology of the Mediterranean Sea was
99 produced by Hecht et al. (1988) for the Levantine Basin. Picco (1990) was also among the first to
100 describe the WMED between 1909 and 1987. In 2002, the Medar/Medatlas group (Fichaut et al., 2003)
101 archived a large amount of biogeochemical and hydrographic in situ observations for the entire region
102 and used the Variational Inverse Model (VIM; Brasseur, 1991) to build seasonal and interannual gridded
103 fields. In 2006, the SeadataNet EU project integrated all existing data, to provide temperature and
104 salinity regional climatology products for the Mediterranean Sea using VIM as well (Simoncelli et al.,
105 2016), and dissolved inorganic nutrients (nitrate, phosphate and silicate) 6-years centered average from
106 1965 to 2017 are available on the EMODnet chemistry portal (<https://www.emodnet-chemistry.eu/>).
107 Within this context, in this study regional climatological fields of in situ nitrate, phosphate and silicate,
108 using the Data Interpolation Variational Analysis (DIVAnd; Barth et al., 2014) are presented here,
109 providing a high-resolution field contributing to the existing products (Table 1).

110 The aim of this study is to give a synthetic view of the biogeochemical state of the WMED, to evaluate
111 the mean state of inorganic nutrients over 36 years of in situ observations and to investigate upon a
112 biogeochemical signature of the effect of the WMT .

113 The paper is organized as follows, section 2 describes the data sources used and the quality check;
114 section 3 is devoted to the methodology, section 4 presents the main results including a comparison of
115 the new climatology with other products. At the end, we address the change in biogeochemical
116 characteristics before and after WMT.



117 **Table 1.** Overview of the existing inorganic nutrient climatologies in the Western Mediterranean Sea.

Climatology	WOA	EMODnet	BGC-WMED (Present study)
Reference	(Garcia et al., 2019)	(Míguez et al., 2019)	(Belgacem et al., 2021)
Year of release	2018	2018	2021
Parameter	Nitrate/ Phosphate/ Silicate	Nitrate/ Phosphate/ Silicate	Nitrate/ Phosphate/ Silicate
Vertical resolution	Seasonal: 43 levels 0-800m Annual: 102 levels 0-5500m	21 standard depth 0-1100m (nitrate) 0-1500m (phosphate) 0-1500m (silicate)	19 levels 0-1500m
Horizontal resolution	1° latitude longitude grid	1/8°	1/4°
Observation time span	1955-2017	1970 to 2016 (nitrate) 1960 to 2016 (phosphate) 1965 to 2016 (silicate)	1981-2017
Area	Global	Mediterranean Sea	Western Mediterranean Sea
Temporal resolution	Season Decadal	Season 6 year running averages	whole observational period, and two sub-intervals (1981-2004, 2005-2017)
Climatology analysis method/ parameter	Objective analysis	DIVA (Data-Interpolating Variational Analysis) tool	DIVAnd (Data-Interpolating Variational Analysis N-dimension)
Correlation length	-	optimized and filtered vertically and a seasonally averaged profile was used.	optimized and filtered vertically and horizontally
Signal to noise ratio	-	A constant value = 1	A constant value = 0.5
Background field	-	the data mean value is subtracted from the data.	the data mean value is subtracted from the data
Detrending	-	No	No
Advection constraint applied	-	No	No

118

119 **2 Data**

120 The climatological analysis depends on the temporal and spatial distribution of the available in situ data,
 121 and the reliability of these observations. Due to the scarcity of biogeochemical observations in the
 122 WMED, merging and compiling data from different sources was necessary.

123 **2.1 Data Sources**

124 In total, 2253 in situ inorganic nutrient profiles are the base of the biogeochemical climatology of the
 125 WMED (Table 2) that is described here. These profiles cover the period 1981-2017 and come from four
 126 main sources, i.e. the Medar/MEDATLAS (1981-1996, Fichaut et al., 2003), the recently published
 127 CNR_DIN_WMED_20042017 biogeochemical dataset (2004-2017) (Belgacem et al., 2020), the
 128 SeaDataNet data product (2001-2016) and other data collected during MedSHIP programs (Schroeder
 129 et al., 2015), GLODAPv2 (<https://www.glodap.info/>) and CARIMED (<http://hdl.handle.net/10508/11313>)
 130 data products. All datasets are a selection of oceanographic cruises carried out within the framework of
 131 European projects or by regional institutions. Data were chosen to ensure high spatial coverage (Fig. 3).



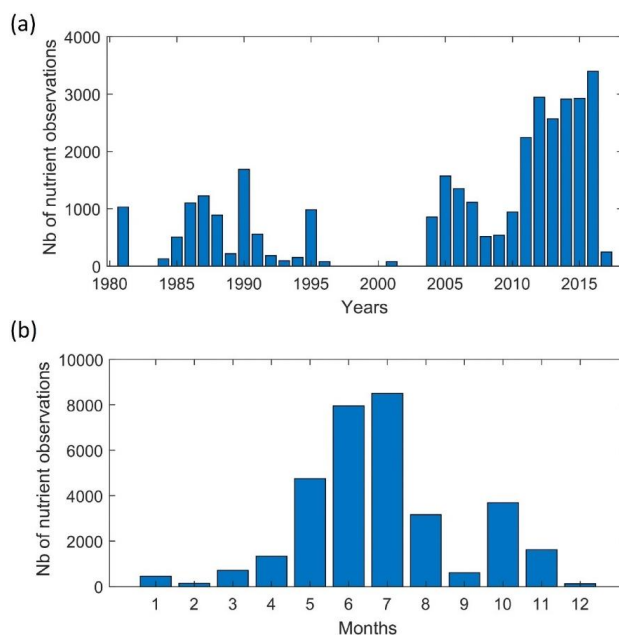
132 **Table 2.** Number of inorganic nutrient profiles and data sources.

Source	N. of profiles	N. of observations	Link
MEDATLAS	940	8839	https://odv.awi.de/data/ocean/medatlasii/
SEADATANET	523	15388	http://seadatanet.maris2.nl/v_rsm/content.asp?screen=0&history=yes
CNR_DIN_WMED_20042017	737	8324	https://doi.org/10.1594/PANGAEA.904172
Other cruises	53	515	Medship programs; GLODAPv2; CARIMED (not yet available online, personal communication by Marta Álvarez)
Σ	2253	33066	-

133

134 2.2 Data distribution

135 The data distribution per year is shown in Figure 2a. Most observations were collected between 1981
 136 and 1995, and between 2004 and 2017, with a marked gap between 1997 and 2003. Measurement
 137 distribution differs from month to month (Fig.2b) and tends to be biased towards the warm season. Very
 138 few measurements have been made during December-January-February, while June and July are the
 139 months with the highest number of available observations (>7000). Consequently, the climatological
 140 product may be considered as being more representative of spring and summer conditions.



141

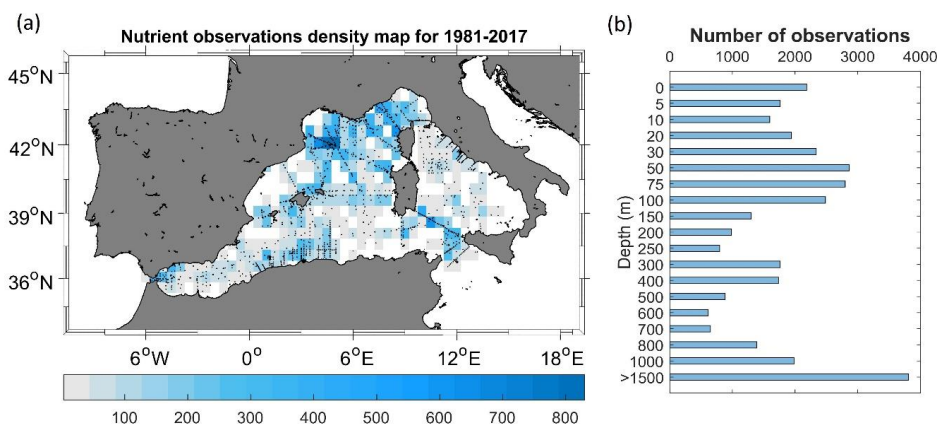
142 **Figure 2.** Temporal distribution of nutrient observations used for producing the BGC-WMED fields
 143 (1981-2017), (a) yearly distribution and (b) monthly distribution.



144 Fig. 3a shows the regional distribution of nutrient measurements, while Fig. 3b indicates the number of
145 observations found in each depth range around the standard levels chosen for the vertical resolution of
146 the climatology.

147 Hydrological and biogeochemical measurements have always been repeatedly collected along several
148 repeated transects, known as key regions as the Sicily Channel and the Algéro-Provençal subbasin;
149 likewise, the northern WMED is a well sampled area, as it is an area of DW formation. Observation
150 density is still scarce (less than 100 observations) in some areas like the northern Tyrrhenian Sea.

151 The total number of measurements at each depth range underlines similar remarks, an uneven
152 distribution that needs to be considered in the selection of the vertical resolution to estimate the
153 climatological fields. Though, the use of 36 years of nutrient measurements to generate the
154 climatological fields significantly reduces the error field. In our case and taking into account the irregular
155 distribution in seasons and different years. A climatological gridded field was computed by analyzing
156 observations of three time periods regardless of the month: 1981-2017 and the subsets 1981-2004 and
157 2005-2017. We chose these subsets to investigate the effect of the WMT on nutrient distribution.



158
159 **Figure 3.** (a) Nutrient data density used for climatology analysis. Observations are binned in a regular
160 $1/2^\circ \times 1/2^\circ$ latitude, longitude grid for each year over the period 1981-2017. Location of the stations
161 included in the analysis are shown as black dots; (b) data distribution per depth range (i.e. at 800 m,
162 observations between 800-1000 m are included).

163 2.3 Data quality check

164 Data were gathered from different data sources, thus before merging them, observations were first
165 checked for duplicate (the number of profiles listed in Table 2 refers to all data after removing duplicate
166 measurements). The criteria to detect and remove duplicate is simple: observations collected during
167 same cruises extracted from the different sources were removed. Since profiles were measured during



168 specific cruise (identified with a unique identification code) at specific time. Data from duplicate cruise
169 are removed.

170 Then, data were converted to a common format (similar to the csv CNR_DIN_WMED_20042017 data
171 product, Belgacem et al., 2019). This recently released product contains measurements covering the
172 WMED from 2004 to 2017. The data of the CNR_DIN_WMED_20042017 product have undergone a
173 rigorous quality control process that was focused on a primary quality check of the precision of the data
174 and a secondary quality control targeting the accuracy of the data. Adjustments were applied to
175 measurements when bias was detected.

176 As detailed in Table 2, we combined observations from reliable sources (covering the time period 1981-
177 2017), that were quality controlled according to international recommendations before being published
178 (Maillard et al., 2007; SeaDataNet Group, 2010). Though, these historical data collections coming from
179 sources different from the CNR_DIN_WMED_20042017 have been subjected to a quality check before
180 merging them, to eliminate the effect of any aberrant observation. The check was carried out by
181 computing median absolute deviations in 19 pressure classes (referring to the selected vertical resolution
182 of section 2.1)(0-10, 10-30, 30-60, 60-80, 80-160, 160-260, 260-360, 360-460, 460-560, 560-900, 900-
183 1200, 1200-1400, 1400-1600, 1600-1800, 1800-2000, 2000-2200, 2200-2400, 2400-2600, >2600 dbar).
184 Any value that is more than three median absolute deviation from the median value is considered a
185 suspected measurement.

186 In total, 2.35% of nitrate observations, 2.44% of phosphate observations and 2.14% of silicate
187 observations were removed.

188 **3 Methods**

189 3.1 Variational analysis mapping tool

190 Here, the **Data-Interpolating Variational Analysis- n dimension** (DIVAnd) method (Beckers et al., 2014;
191 Troupin et al., 2010, 2012) was used to generate the gridded fields. DIVA has been widely applied to
192 oceanographic climatologies, such as the SeaDataNet climatological products (Simoncelli et al., 2014,
193 2016; Iona et al., 2018), EMODnet chemistry regional climatologies (Míguez et al., 2019), the Adriatic
194 Sea climatologies by Lipizer et al. (2014) or the black Sea (Capet et al., 2014) and it was also applied to
195 generate the global interior climatology GLODAPv2. 2016b (Lauvset et al., 2016). It is an efficient
196 mapping tool used to build a continuous spatial field from discrete, scattered, irregular in situ data points
197 with an error estimate at each level.

198 The BGC-WMED gridded fields have been computed with the more advanced N-dimensional version
199 of DIVA, DIVAnd v2.5.1 (Barth et al., 2014) (<https://doi.org/10.5281/zenodo.3627113>) using Julia as



200 a programming language (<https://julia.org/>) under the Jupyter environment (<https://jupyter.org/>).
201 The code is freely available at <https://github.com/gher-ulg/DIVAnd.jl> (last access: January, 2020).

202 DIVA is based on the variational inverse method (VIM) (Brasseur et al., 1996). It takes into account the
203 errors associated with the measurements and takes account of the topography/bathymetry of the study
204 area. The method is designed to estimate an approximated field φ close to the observations and find the
205 field that minimizes the cost function $J[\varphi]$.

206 The cost function is defined as the misfit between the original data d_i , an array of N_d observations, the
207 analysis (observation constraint term) and a smoothness term. (Troupin et al., 2010):

$$208 \quad J[\varphi] = \sum_{i=1}^{N_d} \mu_i Lc^2 (d_i - \varphi(x_i, y_i))^2 \quad (1) \text{ Observation constraint term}$$

$$209 \quad + \int_D (\alpha_2 \nabla \nabla \varphi : \nabla \nabla \varphi + \alpha_1 Lc^2 \nabla \varphi \cdot \nabla \varphi + \alpha_0 Lc^4 \varphi^2) dD \quad (2) \text{ Smoothness term}$$

210

211 Eq. (1)

212 where Lc is the correlation length, ∇ is the gradient operator, $\nabla \nabla \varphi : \nabla \nabla \varphi$ is the squared Laplacian of φ ,
213 the first term (observation constraint) considers the distance between the observations and the analysis
214 reconstructed field, so that μ_i penalizes the analysis misfits relative to the observations. The second term
215 (smoothness term) measures the regularity of the domain of interest D . This expression within the
216 integral remain invariant (Brasseur and Haus, 1991). α_0 minimize the anomalies of the field itself, α_1
217 minimize the spatial gradients, α_2 penalizes the field variability (regularization). The reconstructed
218 fields are determined at the elements of a grid on each isobath using the cost function Eq. (1).

219 The grid is dependent on the correlation length and the topographic contours of the specified grid in the
220 considered region, so there is no need to divide the region before interpolating.

221 The method computes two-, three- to four-multi-dimensional analyses (longitude, latitude, depth, time).
222 For climatological studies, the four-dimensional extension was used on successive horizontal layers at
223 different depths for the whole time period.

224 Along with the gridded fields, DIVA yields error fields dependent on the data coverage and the noise in
225 the measurements (Brankart and Brasseur, 1998; Rixen et al., 2000). Full details about the approach is
226 provided extensively by Barth et al. (2014) and Troupin et al. (2018) in the Diva User Guide.



227 3.2 Interpolation parameters

228 DIVAnd is conditioned by topography, by the spatial correlation length (L_c) and by the signal-to-noise
229 ratio (SNR, λ) of the measurements, which are essential parameters to obtain meaningful results. They
230 are considered more in detail in the following sections.

231 3.2.1 Land-sea mask

232 A 3D dimension land-sea mask is created using the coastline and bathymetry of the General Bathymetric
233 Chart of the Oceans (GEBCO) 30-sec topography (Weatherall et al., 2015). The WMED is a relatively
234 small area which necessitates a high-resolution bathymetry to generate a mask at different depth layers.
235 The vertical resolution is set to 19 standard depth levels from the surface to 1500 m: 0, 5, 10, 20, 30, 50,
236 75, 100, 150, 200, 250, 300, 400, 500, 600, 700, 800, 1000, 1500 m, corresponding to the most
237 commonly used predefined levels for the sampling of seawater for nutrient analyses. The resulting fields
238 at each depth level are the interpolation on the specified grid. These depth surfaces are the domain on
239 which the interpolation is performed.

240 3.2.2 The spatial correlation length scale (L_c)

241 L_c indicates the distance over which an observation affects its neighbors. The correlation length can be
242 set by the user or computed using the data distribution.

243 For the BGC-WMED biogeochemical climatology, this parameter was optimized for the whole-time
244 span, and at each depth layer. The correlation length has been evaluated by fitting the empirical kernel
245 function to the correlation between data isotropy and homogeneity in correlations. The quality of the fit
246 is dependent on the number of observations (Troupin et al., 2018). The analytical covariance model used
247 in the fit is derived for an infinite domain (Barth et al, 2014). To assess the quality of the fit, the data
248 covariance and the fitted covariance are plotted against the distance between data points (Fig. 4). At 10
249 m, the correlation length was obtained with a high number of data points, indicating that the empirical
250 covariance used to estimate the covariance and the fitted covariance are in good agreement.

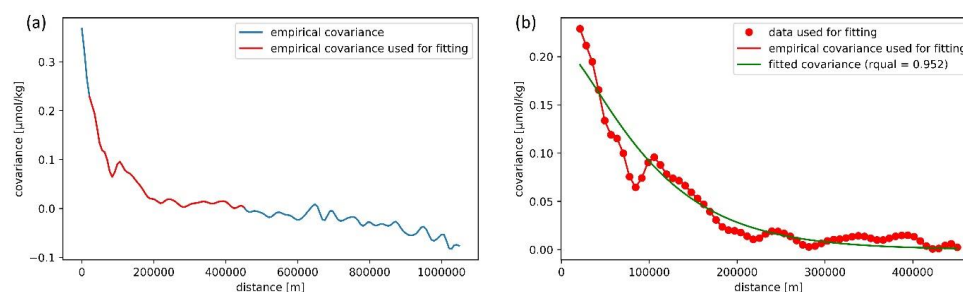
251 At some depth layers there are irregularities due to an insufficient amount of data points, making it
252 necessary to apply a smoothing filter/fit to minimize the effect of these irregularities. It has been tested
253 whether a randomly selected field analysis (nitrate data from 2006 and 2015) obtained with the fitted-
254 vertical correlation profile is better than the analysis with zero-vertical correlation. A skill score relative
255 to analysis non-fitted-vertical correlation has been computed following Murphy (1988) and Barth et
256 al.(2014):

$$257 \textit{skill score} = 1 - \frac{RMS_{no\ fit}^2}{RMS^2} \quad \text{Eq. (2)}$$

258 A large difference in the global RMS between the analysis with the fitted-vertical correlation and the



259 analysis with non-fitted-vertical correlation used for validation was found. The test shows whether the
260 use of the fit in the correlation profile is improving the overall analysis or not. We found that the RMS
261 error was reduced from $0.696 \mu\text{mol kg}^{-1}$ (analysis without fit) to $0.571 \mu\text{mol kg}^{-1}$ (analysis with fit),
262 which means using the fitted vertical correlation profile in the analysis improves the skill by 32 %, and
263 the fit is improving the analysis fields.



264

265 **Figure 4.** Example of the Nitrate covariance. (a) The empirical data covariance function is given in red,
266 curve comes from the analysis of observations within depth = 10 m, while (b) the fitted covariance curve
267 (theoretical kernel) is given in green.

268 Based on the data, DIVA performs a least-square fit of the data covariance function with a theoretical
269 function. Then, a vertical filter is applied and an average profile over the whole period is used (Fig. 5).
270 This procedure is analogous to what has been used for the EMODnet climatology and the North Atlantic
271 climatology, except that in EMODnet climatology, seasonally averaged profiles were used (Buga et al.,
272 2019) and a monthly averaged profiles were used in North Atlantic climatology (Troupin et al., 2010).
273 The filter is applied to discard aberration caused by outliers or scarce observations in some layers, as
274 described above.

275 Because of the horizontal and vertical inhomogeneity of the data coverage, the analysis was based on a
276 correlation length that varies both horizontally (Fig. 5a) and vertically (Fig. 5b).

277 As expected, L_c increases with depth (Fig. 5), extending the influence area of the observation, a
278 consequence of the fact that variability at depth is lower and that observations in the deep layer are
279 scarcer (which on the other hand makes the L_c estimate more uncertain).

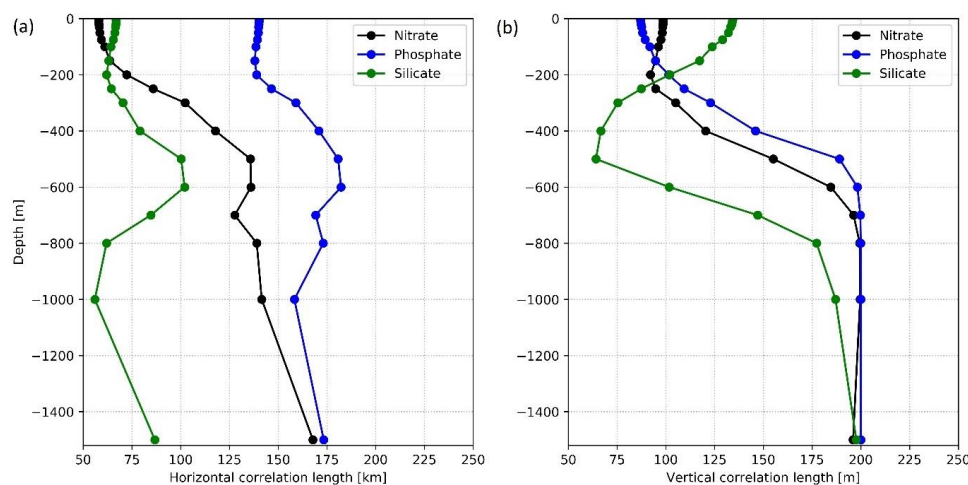
280 From the surface to 150-200 m, L_c is rather constant, while from 200 to 600 m, the horizontal L_c
281 increases for all nutrients. The vertical L_c behaves similarly, for nitrate and phosphate, due to the
282 homogeneity of the intermediate water mass, as explained also by Troupin et al. (2010). For silicate, the
283 vertical L_c decreases in the intermediate depth, reaching a minimum at 500 m depth. The different
284 behavior of silicate could be explained by the progressive increase in concentrations from the surface
285 to the deep layer, compared to nitrate and phosphate vertical distribution (strong gradient between surface
286 depleted layer and intermediate layer). Silicate is less utilized by primary producers, and the dissolution



287 of the biogenic silica is slower than that of the other nutrients (DeMaster, 2002) which explain its
288 progressive increase towards deeper layers (Krom et al., 2014).

289 Below 600 m, the horizontal Lc for silicate decreases down to 1000 m, and then increases again at 1500
290 m. For nitrate and phosphate, a similar, but less marked, behavior is observed. The vertical Lc for all
291 nutrients increases progressively from 400 m to 1500 m.

292 Troupin et al. (2010) and Iona et al. (2018) attributed similar changes observed in Lc for temperature
293 and salinity to the variability of the water masses in each layer. This might also explain the changes
294 found in Lc for nutrients. Indeed, the concentration of nutrients in the WMED increases with depth and
295 is very low at the surface, which explains the constant low values of Lc in this layer.



296
297 **Figure 5.** (a) Horizontal and (b) vertical optimized correlation lengths, for each nutrient (1981-2017),
298 as a function of depth.

299 3.2.3 Signal-to-Noise Ratio

300 The signal-to-noise ratio (SNR) is related to the confidence in the measurements. It is the ratio between
301 the variance of the signal and the variance of the measurement noise/error. The SNR defines the
302 representativeness of the measurements relative to the climatological fields, in other words it is the
303 confidence in the data.

304 It not only depends on the instrumental error but also on the fact that observations are instantaneous
305 measurements, and since a climatology is a long-term mean, such observations do not represent exactly
306 the same.

307 Generally, small SNR values, favor large deviations from the real measurements to give a smoother
308 climatological field. On the other hand, with a high SNR, DIVAnd keeps the existing observations and



309 interpolates between data points. The need is to find an approximation that does not deviate much from
310 the real observations (further details in Lauvset et al., 2016, and Troupin et al., 2010).

311 Following the same approach that many climatologies that used the DIVAnd method adopted, i.e.
312 EMODnet climatologies (available on the EMODnet chemistry portal), the Atlantic regional
313 climatologies (Troupin et al., 2010), the Adriatic Sea climatology (Lipizer et al., 2014) and the
314 SeadataNet regional climatology (Simoncelli et al., 2015), the SNR is set to a constant value (Table 1).

315 The analysis is performed with a predefined uniform default error variance of 0.5 for all parameters at
316 all depths. Three iterations are done inside DIVAnd to estimate the optimal scale factor of error variance
317 of the observation (following Desroziers et al., 2005). More details can be found in [https://gher-
318 ulg.github.io/DIVAnd.jl/latest/#DIVAnd.diva3d](https://gher-
318 ulg.github.io/DIVAnd.jl/latest/#DIVAnd.diva3d).

319 Values of SNR provided by means of a generalized cross-validation (GCV) technique (Brankart and
320 Brasseur, 1998) gave a large estimate of the SNR (of the order of 22) showing a discontinuous analysis
321 field and patterns around the cruise transects and do not represent properly the climatological fields.

322 High SNR means less confidence in the observation, while we presume that the data sources used to
323 generate BGC-WMED climatology are consistent products.

324 3.3 Detection of suspicious data

325 Assessment of the analysis is performed by detecting outliers and suspicious data, in order to remove
326 observations that generate irregular interpolated fields and suspect observations that were not detected
327 in the data quality check of section 2.3.

328 The automatic check measures how consistent the gridded field is with respect to the nearby
329 observations by estimating the difference between a measurement and its analysis scaled by the expected
330 error and, based on that, a score is assigned to each observations. Data points with high scores were
331 considered as suspect and were removed from the analysis. Overall, 0.031%, 0.014%, 0.004% data
332 points, for nitrate, phosphate, and silicate, respectively, were considered inconsistent. The quality check
333 values that were used are available in the netCDF files of the product.

334 3.4 Quality check of the analysis fields

335 The quality of the climatology was checked against observations by estimating the mean residual and
336 RMS of the difference between the climatology and the observations. Averages over the entire basin
337 were calculated between depth levels (see section 2.3).

338 Residuals are the difference between the observations and the analysis (interpolated linearly to the
339 location of the observations). The residuals are NaN when the observations fall outside the selected
340 domain for the climatology, as defined by the mask and the coordinates of the observations

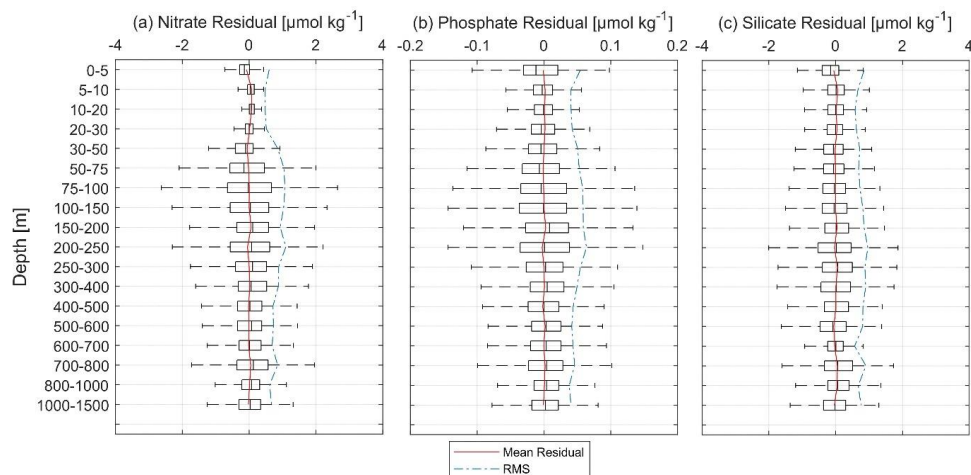


341 The result of Fig. 6a shows nitrate residuals. From the 0 to 30 m depth, the observations and the analysis
342 have a high level of agreement. Between 30 and 200 m, boxplots are suggestive of larger differences.
343 From surface to the deep layer, the mean residual varied between -0.075 and $0.0765 \mu\text{mol kg}^{-1}$. The
344 RMS for nitrate varied between 0.47 and $1.1 \mu\text{mol kg}^{-1}$.

345 As for phosphate residuals (Fig. 6b), low level of agreement was found between 75 and 200 m and a
346 lower difference in the surface and below 250 m. The average residual varied between -0.0027 and
347 $0.0026 \mu\text{mol kg}^{-1}$. The RMS for phosphate varied between 0.037 and $0.063 \mu\text{mol kg}^{-1}$.

348 Silicate residuals (Fig. 6c), on the other hand, seemed more homogeneous at all depth levels. The highest
349 level of agreement was found below 20 m and at 600 m. Overall residuals varied between -0.057 and
350 $0.063 \mu\text{mol kg}^{-1}$, while the RMS ranged between 0.567 and $0.963 \mu\text{mol kg}^{-1}$.

351 Over the entire water column, the mean residual was around zero ($0.004 \mu\text{mol kg}^{-1}$ for nitrate, 0.0002
352 $\mu\text{mol kg}^{-1}$ for phosphate and $0.003 \mu\text{mol kg}^{-1}$ for silicate) (Fig. 6), meaning that in general, the bias
353 between the observations and the analysis is small.



354

355 **Figure 6.** Vertical mean residuals (in red), i.e. the differences between the observations and the analysis
356 and the mean RMS (dashed blue) of (a) nitrate, (b) phosphate, (c) silicate.

357 4 Results

358 The final result consists of gridded fields of mapped climatological means of inorganic nutrients for the
359 periods 1981-2004, 2005-2017, and the whole period 1981-2017, produced with VIM described in
360 section 3, using data of section 2. Together with the gridded fields, error maps have been generated to
361 check the degree of reliability of the analysis.



362 The resulting climatologies (Table 3) are aggregated in a 4D netCDF for each nutrient and each time
363 period that contains the interpolated field of the variable and related information: associated relative
364 error, variable fields masked using two relative error thresholds (L1 and L2). The mapped climatology
365 is available from PANGAEA (<https://doi.pangaea.de/10.1594/PANGAEA.930447>, Belgacem et al.,
366 2021) as one folder named BGC-WMED climatology. This folder contains nine netCDF files for each
367 parameter and time period.

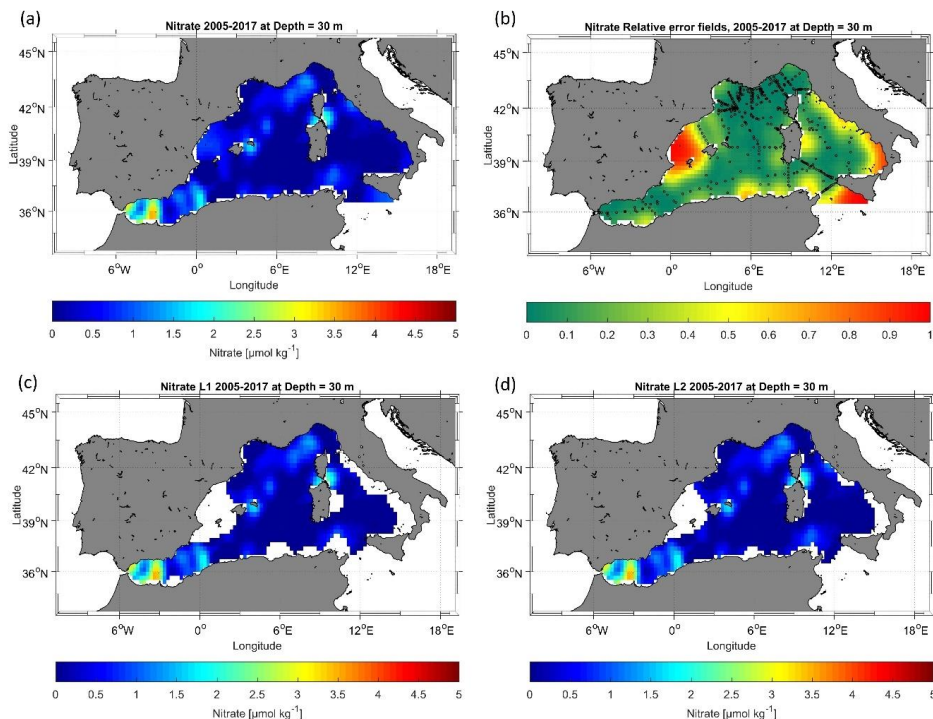
368 Here is an example of the analysis output found in the netCDF. Figure 7 shows the unmasked
369 climatological field of the mean spatial variation of nitrate, relative error field distribution, the masked
370 climatological field using relative error with two threshold values (0.3 and 0.5) to assess the quality of
371 the resulting fields.

372 **Table 3.** Available analyzed fields and available information in the netCDF files.

Variable name	Field name	Description
Lon	Longitude	Longitude in degrees east, extent: -7 – 17.25 °E
Lat	Latitude	Latitude in degrees north, extent: 33.5 – 45.85°N
depth	Depth	Depth in meters, 19 levels, range: 0 – 1500 m
nitrate/phosphate/silicate	DIVAnd analyzed climatology	Mapped climatological fields
nitrate_L1/phosphate_L1/ silicate_L1	Nitrate/Phosphate/Silicate masked field level 1	Mapped climatological fields masked using relative error threshold 0.3.
nitrate_L2/ phosphate_L2/ silicate_L2	Nitrate/Phosphate/Silicate masked field level 2	Mapped climatological fields masked using relative error threshold 0.5.
nitrate_relerr/phosphate_re lerr/silicate_relerr	Nitrate/Phosphate/Silicate masked relative error	Mapped relative error filed associated to the climatological field



373



374

375 **Figure 7.** Example of nitrate analysis for the period 2005-2017 (a) unmasked analysis field, (b) relative
376 error field distribution with the observation in black circles, (c) masked analysis fields masked using
377 relative error threshold = 0.3, and (d) masked analysis fields masked using relative error threshold = 0.5.

378 4.1 Nutrient climatological distribution

379 A description of the spatial patterns of the dissolved inorganic nutrients across the domain and over the
380 entire period (1981-2017) is given. The gridded fields for nitrate, phosphate, and silicate are discussed
381 at three depth levels, representative of the surface (at 100 m), intermediate (at 300 m), and deep layer
382 (at 1500 m). The horizontal maps at the selected depths are shown in Fig. 8, while the average vertical
383 profiles of nutrients over the whole area are shown in Fig. 9.

384 4.1.1 Surface layer

385 The nitrate, phosphate and silicate mean climatological fields over 1981-2017 are presented in Fig. 8
386 (a, b, c) respectively. The mean surface nitrate at 100 m is about $3.58 \pm 1.16 \mu\text{mol kg}^{-1}$. Highest surface
387 values of nitrate concentrations are found in regions where strong upwelling or vertical mixing occurs,
388 such as the Liguro-Provençal basin and the Alboran Sea (see Fig. 8a).



389 The convection region (Gulf of Lion and Ligurian Sea) is characterized by an eutrophic regime and a
390 spring bloom (Lavigne et al., 2015), unlike the rest of the basin that shows low nitrate concentrations in
391 the surface layer ($< 4 \mu\text{mol kg}^{-1}$).

392 Nutrient patterns in the Alboran Sea have been associated with the distinct vertical mixing that supplies
393 the surface layer with nutrients (Lazzari et al., 2012; Reale et al., 2020).

394 Indeed, the northern Alboran Sea is known as an upwelling area, where permanent strong winds enhance
395 the regional biological productivity (Reul et al., 2005). Nitrate distribution at 100 m presents a clear
396 distinction between the enriched surface regions in the WMED, under the influence of deep convection
397 processes, and the easternmost depleted region.

398 The distribution of phosphate concentration has striking similarities with that of nitrate (Fig. 8b). The
399 mean surface phosphate concentrations at 100 m, is $0.16 \pm 0.06 \mu\text{mol kg}^{-1}$. As for nitrate, the highest
400 surface values are found in the Alboran Sea, Balearic Sea, Gulf of Lion and Liguro-Provençal Basin
401 ($0.2\text{-}0.3 \mu\text{mol kg}^{-1}$), while the Tyrrhenian Sea and the Algerian Sea revealed phosphate concentration
402 that were $<0.2 \mu\text{mol kg}^{-1}$. Similar patterns were observed by Lazzari et al. (2016), who argued that the
403 variations in phosphate are regulated by atmospheric and terrestrial inputs. It should be noted that the
404 maximum in the surface is found near river discharges of freshwater, like Ebro and Rhône, i.e. the largest
405 rivers of the WMED (Ludwig et al., 2009).

406 Concerning the distribution of silicate concentration, the surface layer at 100 m (Fig. 8c) followed the
407 same pattern as nitrate and phosphate. Over this layer the mean silicate was about $2.7 \pm 0.7 \mu\text{mol kg}^{-1}$.
408 As for nitrate and phosphate, the highest values ($3\text{-}4 \mu\text{mol kg}^{-1}$), were recorded in the Alboran Sea,
409 Balearic Sea, Gulf of Lion and Liguro-Provençal Basin and in the southern entrance of Tyrrhenian Sea.
410 This surface distribution is in good agreement with the findings of Crombet et al. (2011), relating this
411 local silicate surface maximum to the continental input, river discharge and atmospheric deposition
412 (Frings et al., 2016; Sospedra et al., 2018). The spatial minima were reported in the Tyrrhenian Sea and
413 Algerian Sea ($<3 \mu\text{mol kg}^{-1}$).

414 4.1.2 Deep and Intermediate layer

415 At the basin scale, nitrate concentrations increase with depth (Fig. 9a), with the highest concentration
416 found at intermediate levels (250-500 m), ranging between 8.8 and $9.0 \mu\text{mol kg}^{-1}$. In this 300 m (Fig.
417 8d), nitrate concentrations average is $7.2 \pm 1.06 \mu\text{mol kg}^{-1}$. High values ($> 6.5 \mu\text{mol kg}^{-1}$) are found in
418 the westernmost regions (Alboran Sea, Algerian Sea, Gulf of Lion, Balearic Sea and the Liguro-
419 Provençal Basin), while the easternmost regions (Tyrrhenian Sea, Sicily Channel), exhibit much lower
420 concentrations (between 4.5 and $6.5 \mu\text{mol kg}^{-1}$).

421 Similar features are observed in the deep layer, at 1500 m (Fig. 8a), with nitrate concentrations
422 increasing all over the basin, reaching on average $7.8 - 7.9 \mu\text{mol kg}^{-1}$ between 1000 and 1500 m depth
423 (Fig. 9a).



424 In both layers (300 m and 1500 m), the difference between the eastern opening of the basin (Sicily
425 Channel) and the western side (Alboran Sea) is noticeable: the Sicily Channel and the Tyrrhenian Sea
426 are under the direct influence of the water masses coming from the oligotrophic EMED, which then
427 gradually become enriched with nutrients along its path, as found by Schroeder et al. (2020).
428 Phosphate concentrations at intermediate depth (see 300 m, Fig. 8e), varied between 0.12 and 0.44 $\mu\text{mol kg}^{-1}$,
429 and the horizontal map shows the same gradual decrease towards east, with the highest
430 concentrations in the westernmost regions and minimum values in the eastern regions ($< 0.25 \mu\text{mol kg}^{-1}$).
431
432 The average vertical profile over the entire region (Fig. 9b), reveals a maximum in phosphate
433 concentrations between 300 and 800 m depth, related to an increased remineralization process.
434 In the deep layer (see 1500 m, Fig. 8h), phosphate concentration average is $0.36 \pm 0.02 \mu\text{mol kg}^{-1}$.
435 Generally, the deep layer is homogeneous (Fig. 9b). The difference observed between westernmost
436 regions and the Tyrrhenian Sea remains, though the latter demonstrate higher phosphate concentrations
437 ($\sim 0.3 \mu\text{mol kg}^{-1}$). This variation could be due to the difference in the water masses. The IW inflow from
438 the EMED brings relatively young waters that are depleted in nutrients, while in the higher
439 concentrations in the deep layer are signatures of the older resident DW of the Tyrrhenian. The change
440 in the biological uptake in the intermediate source water could explain the regional variability of
441 nutrients. The low productivity (D'Ortenzio and Ribera d'Alcalà, 2009) and the pronounced
442 oligotrophic regime of EMED water (Lazzari et al., 2016) may justify the increase in nutrients in the
443 IW.
444 Silicate concentration distribution at intermediate (300 m, Fig. 8f) and deep layers (1500 m, Fig. 8i),
445 were as expected, showing a notable increase, compared to the surface. Here the silicate average
446 concentration is $5.83 \pm 0.66 \mu\text{mol kg}^{-1}$. The maximum values were observed below 800 m, $> 8.034 \mu\text{mol kg}^{-1}$
447 (Fig. 4.9c). At 1500 m, silicate distribution is homogeneous all over the basin (on average $8.35 \pm$
448 0.39).
449 Generally, primary producers do not require silicate for their growth as much as they need nitrate and
450 phosphate which explain the disparity between nutrients patterns. Furthermore, at intermediate levels,
451 the water is warmer than at deep levels, enhancing the dissolution rate and the progressive increase in
452 silicate (DeMaster, 2002). The biogenic silicate is exported to greater depths and continues to dissolve
453 generating inorganic silicate as it sinks to the bottom. The recycling of silicate within the deep-sea
454 sediments is later on redistributed by the deep currents which explain the homogenous horizontal
455 distribution over the entire basin.
456 Comparing the three nutrients at the same depth levels, at the surface (100 m), it appears that they all
457 show local surface maximum, depending on local events such as strong winds, local river discharge and,
458 vertical mixing (Ludwig et al., 2010).
459 In the easternmost areas, the surface depletion in nutrients (Van Cappellen et al., 2014) is attributed to
460 the variation in the thermohaline properties that has impacted primary production (Ozer et al., 2017) and



461 the export of organic matter to intermediate and deep layers leading to the accumulation of nutrients in
462 these depth ranges.

463 The Tyrrhenian sea is not directly connected to convection regions. Here, the EMED water inflow plays
464 a major role. Li and Tanhua (2020) found an increased ventilation of the intermediate and deep layers
465 during 2001 to 2018 in the Sicily channel and a constant AOU between 2001-2016, suggesting a constant
466 ventilation that explain the peculiar nutrient distribution in that area. In the western side of the WMED,
467 intermediate and deep layers exhibit an increase in nutrients. Schroeder et al. (2020) explained this
468 increase in nitrate and phosphate at the intermediate layer with the increase of the remineralization rate
469 at these depths along the path of IW.

470 The deficiency of inorganic nutrients is explained by the effect of the anti-estuarine circulation, with the
471 IW coming from the EMED, which is known to be poor in nutrients (Krom et al., 2014; Schroeder et
472 al., 2020), accumulates nutrient along its path. Thus, this relative nutrient-rich Mediterranean outflow is
473 lost to the Atlantic Ocean.

474 Overall, in surface layer, circulation, physical processes, and vertical mixing increase nutrient input
475 while the biological pump controls the decrease.

476 In the deep layer, the variability is lower (standard deviation is reduced toward the bottom for all three
477 nutrients, see Fig.9), the deep layer accumulates dissolved organic nutrients. In the WMED, the deep
478 layer constitutes a reservoir of inorganic nutrients.

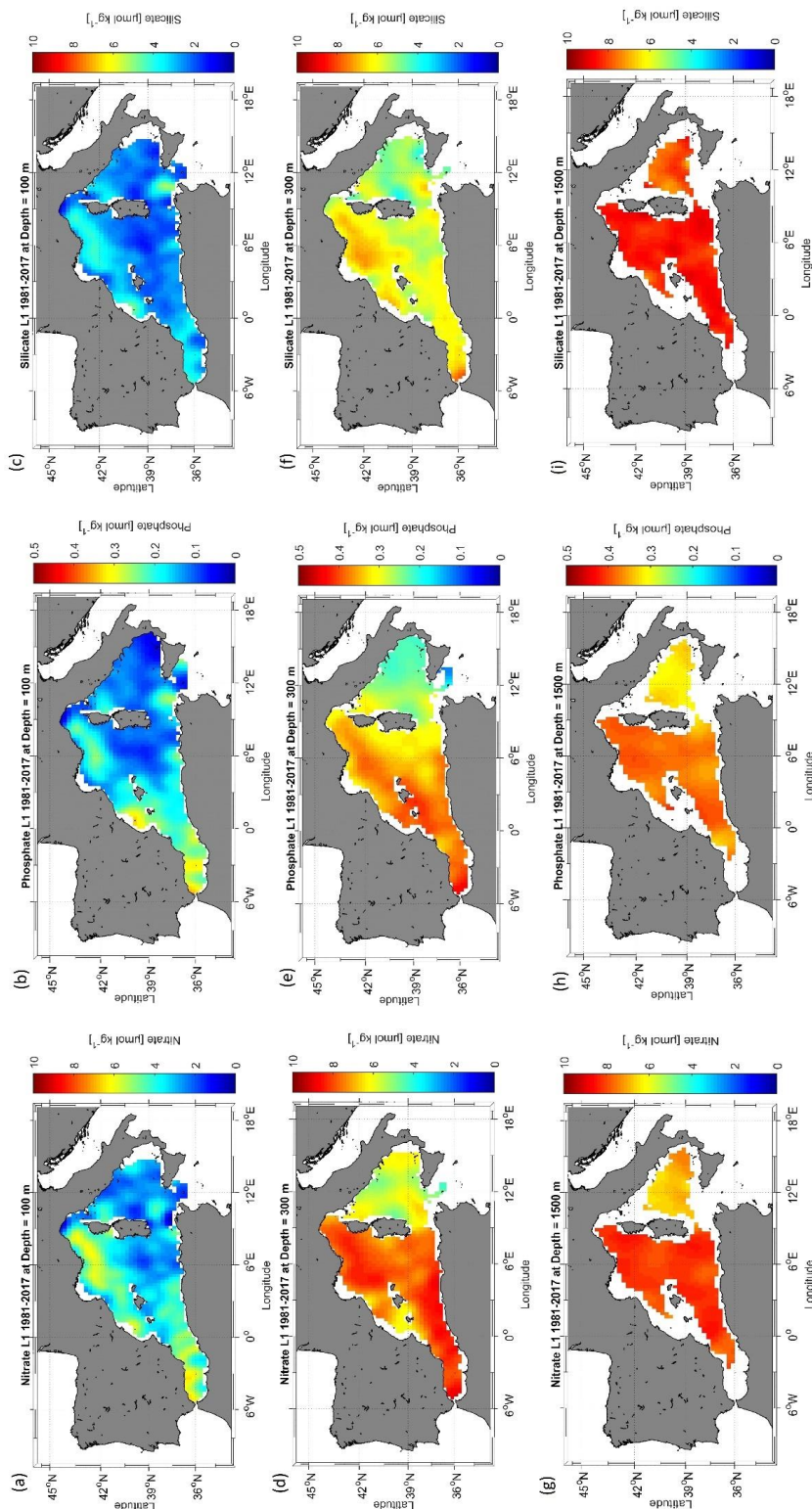
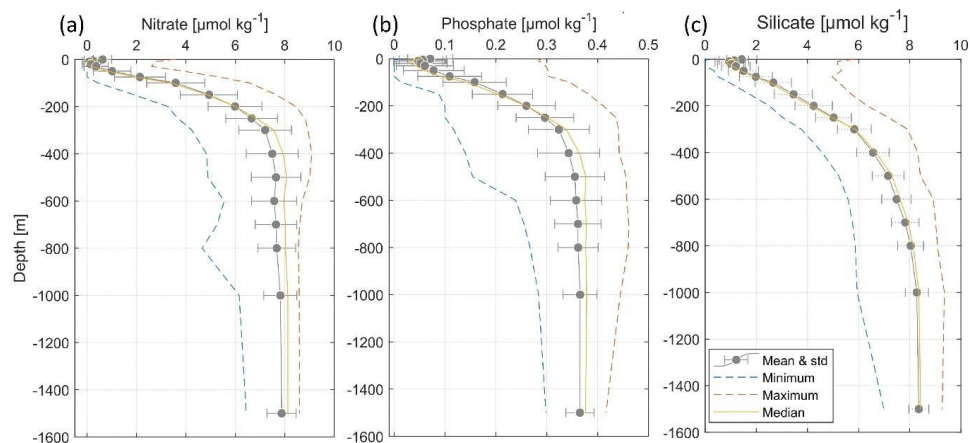


Figure 8. Climatological map distribution of nitrate (a. at 100 m, d. at 300 m, g. at 1500 m), phosphate (a. at 100 m, d. at 300 m, g. at 1500 m) and silicate (a. at 100 m, d. at 300 m, g. at 1500 m) for the period from 1981 to 2017.



479



480

481 **Figure 9.** Climatological mean vertical profiles of (a) nitrate, (b) phosphate and (c) silicate
482 concentrations in the WMED (1981-2017). Dashed blue line indicates the minimum, dashed orange line
483 indicates the maximum, continuous yellow line indicates median profile, error bars and mean profile are
484 in grey.

485 4.2 Error fields

486 The determination of the error field is important to gain insight in the confidence in the climatological
487 results. Mostly, the error estimate depends on the spatial distribution of the observations and the
488 measurement noise. In DIVAnd, there are different methods available to estimate the relative error
489 associated with the analysis fields.

490 A climatological field is computed at several depths (19 levels in this case), for different parameters
491 (nitrate, phosphate, and silicate in this case). Given these premises and following the approach of similar
492 climatologies (GLODAPv2.2016b, Lauvset et al., 2016; SeaDataNet aggregated data sets products,
493 Simoncelli et al., 2015), for the BCG-WMED the error fields were estimated using the default DIVAnd
494 method, i.e. the “clever poor man's error approach”, a less time consuming but efficient computational
495 approach. According to Beckers et al. (2014) who also provide details about the mathematical
496 background of the error fields computation, this method appropriately represents the true error and
497 provides a qualitative distribution of the error estimate. This estimate is used to generate a mask over
498 the analysis fields. Two error thresholds were applied (0.3 (L1) and 0.5 (L2)). Fig.7b., show the main
499 error that occurs in region void from measurements. An example of the analysis masked with the error
500 thresholds output is shown in Fig.7c (L1) and Fig.7d (L2). The associated error fields with the analysis
501 fields are integrated in the data product.



502 4.3 Comparison with other biogeochemical data products

503 In this section a comparison of the BGC-WMED product with the most known global and/or regional
504 climatologies, that are frequently used as reference products for initializing numerical models, is done.

505 Specifically, the analyzed fields are compared to the reference data products WOA18 (Garcia et al.,
506 2019) and the reanalysis of the Mediterranean Sea biogeochemistry, medBFM, a CMEMS product
507 (Teruzzi et al., 2019). Since the products used for inter-comparison were not originated from the same
508 interpolation method, not for the same time period and with different spatial resolution, here the
509 comparison is mostly targeted on the general patterns of nutrients in the region.

510 Comparisons are carried out between horizontal maps (Fig.10-11-12), as well as along a vertical
511 longitudinal transect (Fig.14-15). In addition, following Reale et al. (2020), the first 150 m have been
512 evaluated (Fig.13), since this is a depth level with a representative amount of in situ observations in all
513 three products. The evaluation is based on the estimation of horizontal average, on BGC-WMED
514 climatology, the medBFM biogeochemical reanalysis and the WOA18 climatology by subregion. i.e. a
515 spatial subdivision made according to Manca et al. (2004).

516 Products have different grid resolution, thus to compare between them, the BGC-WMED new
517 climatological data product (at $0.25^\circ \times 0.25^\circ$) for periods 1981-2017 and 2005- 2017 and the medBFM
518 biogeochemical reanalysis (at $0.063^\circ \times 0.063^\circ$) (Teruzzi et al. 2019)
519 (https://doi.org/10.25423/MEDSEA_REANALYSIS_BIO_006_008) for the period 2005- 2017, are
520 regridded on the WOA18 ($1^\circ \times 1^\circ$) grid using nearest neighbor interpolation. The regridding is computed
521 at all depth levels of the different products. The MedBFM reanalysis climatological mean was computed
522 for the period 2005-2017 prior the interpolation.

523 4.3.1 Comparison with WOA18 at 150 m

524 Fig. 10-11-12 show the analysis at the 150 m depth surface for the three nutrients. The BGC-WMED
525 (1981-2017) product reveals detailed aspects of the general features of nitrate (Fig. 10.a), phosphate
526 (Fig. 11a) and silicate (Fig.12a).

527 For the three nutrients, the new product reproduces patterns similar to the WOA18 all over the region.
528 It shows well-defined fields and higher values of nitrate and phosphate concentrations. In the new
529 product, nitrate concentrations varied between $2.31 - 7.3 \mu\text{mol kg}^{-1}$ the WOA18 values were $2.19 - 5.99$
530 $\mu\text{mol kg}^{-1}$. Phosphate ranges were similar between the two products between $(0.092 - 0.35 \mu\text{mol kg}^{-1})$
531 (BGC-WMED) and $0.095 - 0.35 \mu\text{mol kg}^{-1}$ (WOA18). Likewise, Silicate range values at 150 m were
532 not different $(2.07 - 4.99 \text{ (BGC-WMED)})$ and $1.57 - 5.75 \mu\text{mol kg}^{-1}$ (WOA18).

533 The average RMS difference (RMSD) calculated from the difference between the WOA18 and BGC-
534 WMED all over the region at 150 m is about $1.14 \mu\text{mol kg}^{-1}$ nitrate (Fig. 10c), $0.055 \mu\text{mol kg}^{-1}$ for



535 phosphate (Fig. 11c) and $0.91 \mu\text{mol kg}^{-1}$ for silicate (Fig. 12c). Overall, the RMS error values were low
536 indicating limited a disparity between the two products.

537 The difference field for every grid point reflects this discrepancy and shows areas with limited
538 agreement between the two products, that can have a difference $>2 \mu\text{mol kg}^{-1}$ for nitrate (Fig. 10c), >0.1
539 $\mu\text{mol kg}^{-1}$ for phosphate (Fig. 11c), $>1.5 \mu\text{mol kg}^{-1}$ for silicate (Fig. 12c). This dissimilarity is also noted
540 with the low r^2 (Fig. 13) (0.34, 0.20, 0.095 for nitrate, phosphate, and silicate respectively)

541 The distribution of the surface nitrate concentrations (at 150m) (Fig. 10a) of the new product is similar
542 to that shown in WOA18 (Fig. 10b). The largest difference between the two products occurs in northwest
543 areas and in the Alboran Sea (Fig. 10c), areas of higher concentrations, a more nutrient rich surface
544 water as described in section 4.1. The difference is pronounced in these regions likely because the new
545 product holds more in situ observations than the WOA18 in the WMED.

546 Phosphate surface concentrations (Fig. 11) show similar differences as nitrate. The largest difference
547 with the surface phosphate of the WOA18 is found in the Alboran Sea, Northern WMED and Sicily
548 region (Fig. 11c).

549 As for silicate, the surface distribution shows large differences (Fig. 12c). The highest values are
550 observed in the northwest area of the new product, and in the Alboran Sea in the WOA18 climatology ,
551 this again accounts for the data coverage difference.

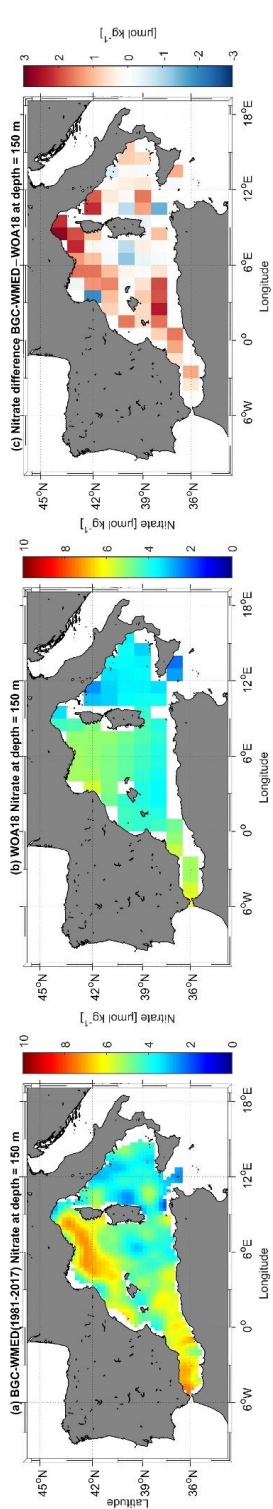


Figure 10. (a) BGC-WMED (1981-2017) nitrate climatological field at 150 m depth (0.25° resolution); (b) WOA18 nitrate climatological field at 150 m depth (1° resolution); (c) difference between BGC-WMED and WOA18 nitrate fields at 150 m (1° resolution).

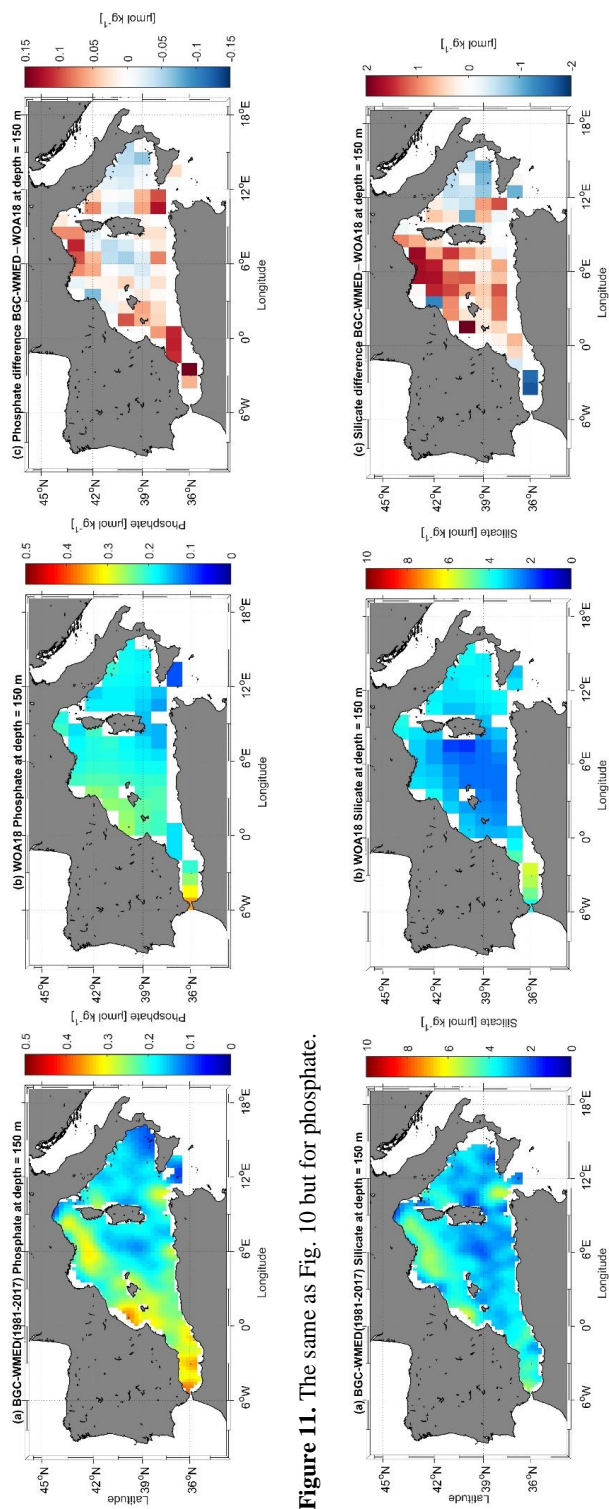


Figure 11. The same as Fig. 10 but for phosphate.

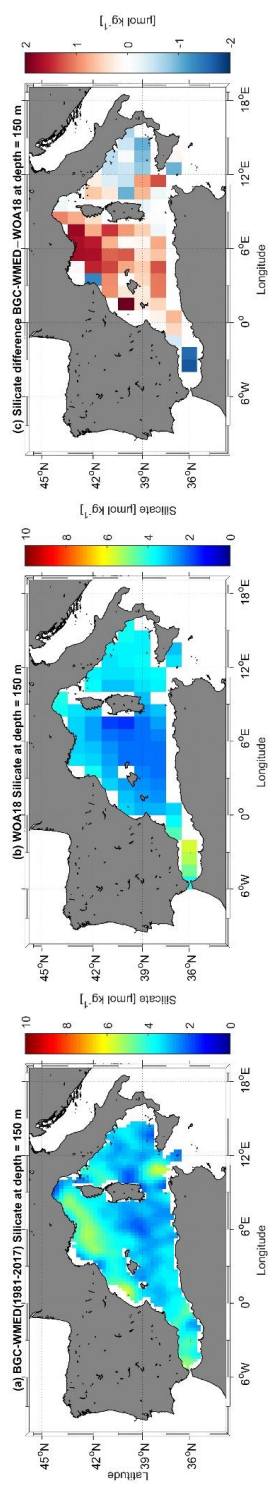


Figure 12. The same as Fig. 10 but for silicate.

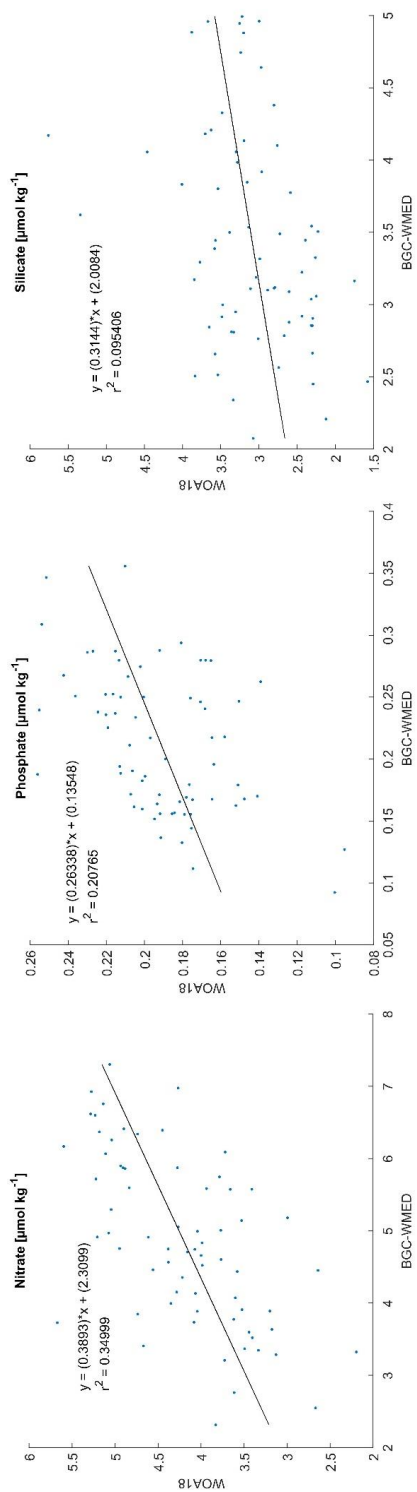


Figure 13. Scatterplot showing the WOA18 data as a function of the BCC-WMED climatology at 150 m with the regression line.



552 4.3.2 Regional horizontal comparison above 150 m average nutrient concentrations

553 The inorganic nutrient mean concentrations resulting from the climatology of this work (period 2005-
554 2017), and from both the medBFM reanalysis product and the WOA18 are compared in the upper layer
555 of 12 subregions of the WMED (in Table 4 and Fig. 14).

556 Results show a general agreement between BGC-WMED and the other two products in some
557 subregions, nonetheless, there are some differences as shown in section 4.3.1.

558 Upper layer nitrate average concentrations (Fig. 14a) are decreasing eastward, from the Alboran Sea
559 (DS1) to the Algerian basin (DS3, DS4) and the Balearic Sea (DS2). The western part of the basin is an
560 area under the direct influence of the inflowing Atlantic surface waters, where nitrate is known to be
561 present in excess compared to phosphate probably due to atmospheric N₂ input (Lucea et al., 2003). In
562 the DS1, BGC-WMED nitrate levels are lower than the WOA18 nitrate levels while in DS3, DS2 and
563 DS4 the average nitrate concentrations are similar to the WOA18.

564 From the Algerian basin (DS4, DF1) to Liguro-Provençal (DF3) regions, there is an increase in the
565 average nitrate in all products, this is the south-north gradient. Some difference arises, where the new
566 product is lower than the WOA18.

567 In the eastern regions, the lowest average concentrations of the WMED are found. Here, the difference
568 between products is smaller, with medBFM reanalysis being lower than the new product and the
569 WOA18.

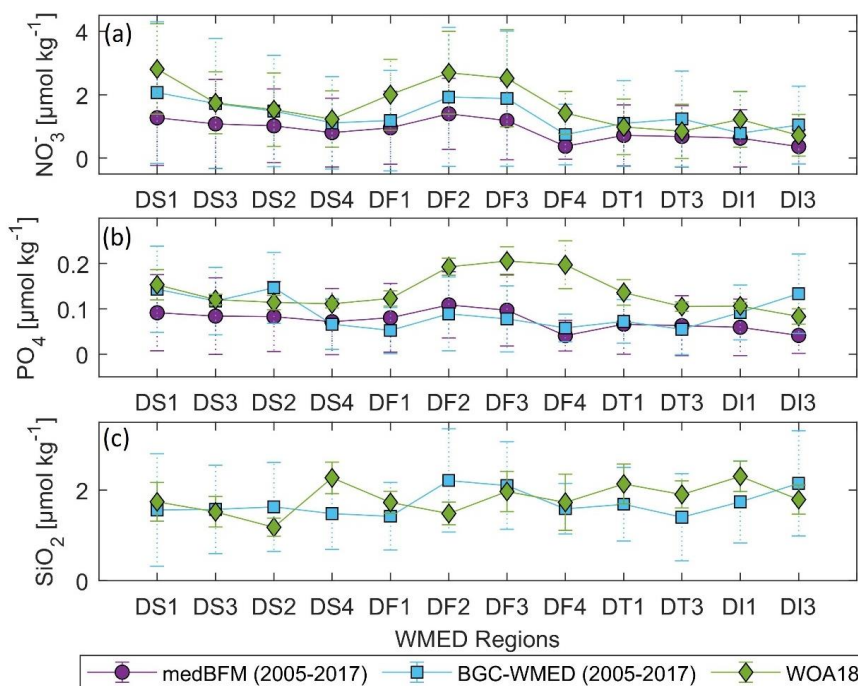
570 As for phosphate (Fig. 14b), known to be the limiting nutrient of the WMED, because it is rapidly
571 consumed by phytoplankton (Lucea et al., 2003), its average levels are low in DS1, DS3, DS2 and DS4,
572 in WOA18, medBFM reanalysis and BGC-WMED. The latter did not agree well with the other products
573 in DS2, where it was slightly higher. Phosphate average concentrations slightly increase in DF1, DF2
574 and DF3 in all three products. The increase is explained by the vertical mixing process occurring in the
575 northern WMED.

576 Upper surface phosphate concentrations average start to decrease progressively through the Ligurian
577 East (DF4), Tyrrhenian Sea (DT1, DT3), Sardinia Channel (DI1) and Sicily Channel (DI3). The BGC-
578 WMED was in agreement with medBFM reanalysis in those subregions aside from concentrations in
579 DI3, where the new product showed higher levels.

580 The BGC-WMED climatology shows reasonable agreement in the upper average concentrations of
581 nitrate and phosphate that are similar in order of magnitude to the other products (Fig. 14). The
582 difference with the WOA18 resides in the wider temporal window of the observation (starting from
583 1955). The new climatology in some subregions has a better spatial coverage of in situ observation than
584 the WOA18 (Garcia et al., 2019) and the medBFM reanalysis (Teruzzi et al., 2019).



585 On the other hand, the average silicate (Fig. 14c) of the new product and the WOA18 varied between
 586 regions. Significant difference is found between the two products in DS2, DS4, DF1, DF2, DT1, DT3,
 587 DI1 and DI3, while in DS1, DS3 and DF4 mean silicate is consistent between the two products.
 588 Overall, the three products show strongly similar features between regions (similar curve shape).



589

590 **Figure 14.** Nutrient average concentrations and standard deviation comparison in the upper 150 m
 591 (values in Table 4).

592

593

594

595

596

597

598

599

600



601 **Table 4.** Nutrient average concentrations and standard deviation in the upper 150 m. All products were
 602 interpolated on 1° grid resolution (see Figure S2 (Belgacem et al., 2020)).

Subregion/ Coverage	Data product	Nitrate	Phosphate	Silicate
<i>DS1- Alboran Sea</i> (35°N– 37.3°N, -6°E– -1°E)	medBFM	1.27(±1.4)	0.09(±0.08)	-
	BGC-WMED	2.06(±2.2)	0.14(±0.09)	1.56(±1.2)
	WOA18	2.81(±1.4)	0.15(±0.03)	1.74(±0.4)
<i>DS3- Algerian West</i> (35.36°N– 38.3°N, -1°E– 4.3°E)	medBFM	1.07(±1.4)	0.08(±0.08)	-
	BGC-WMED	1.72(±2.05)	0.11(±0.07)	1.57(±0.9)
	WOA18	1.74(±0.9)	0.12(±0.01)	1.52(±0.3)
<i>DS2- Balearic Sea</i> (38.3°N– 42°N, -1°E–4.3 °E)	medBFM	1.02(±1.1)	0.08(±0.07)	-
	BGC-WMED	1.48(±1.7)	0.14(±0.07)	1.63(±0.9)
	WOA18	1.53(±1.1)	0.11(±0.01)	1.18(±0.2)
<i>DS4- Algerian East</i> (36.3°N– 39.18°N, 4.3°E– 8.24°E)	medBFM	0.80(±1.08)	0.07(±0.07)	-
	BGC-WMED	1.11(±1.4)	0.06(±0.05)	1.48(±0.7)
	WOA18	1.23(±0.8)	0.11(±0.009)	2.27(±0.3)
<i>DF1- Algero-Provençal</i> (39.18°N– 41°N, 4.3°E– 9.18°E)	medBFM	0.96(±1.15)	0.08(±0.07)	-
	BGC-WMED	1.18(±1.5)	0.05(±0.05)	1.42(±0.7)
	WOA18	2.00(±1.1)	0.12(±0.01)	1.73(±0.2)
<i>DF2- Gulf of Lion</i> (42°N–43.36°N, 1°E–6.18°E)	medBFM	1.39(±1.19)	0.10(±0.07)	-
	BGC-WMED	1.92(±2.1)	0.08(±0.08)	2.21(±1.1)
	WOA18	2.68(±1.3)	0.19(±0.01)	1.48(±0.2)
<i>DF3- Liguro-Provençal</i> (41°N– 45°N, 6.18°E– 9.18°E)	medBFM	1.18(±1.2)	0.09(±0.07)	-
	BGC-WMED	1.88(±2.1)	0.07(±0.07)	2.10(±0.9)
	WOA18	2.52(±1.5)	0.20(±0.03)	1.97(±0.4)
<i>DF4- Ligurian East</i> (42.48°N–45°N, 9.18°E– 11°E)	medBFM	0.37(±0.4)	0.04(±0.03)	-
	BGC-WMED	0.74(±0.9)	0.05(±0.03)	1.59(±0.5)
	WOA18	1.42(±0.6)	0.19(±0.05)	1.73(±0.6)
<i>DT1- Tyrrhenian North</i> (39.18°N–42.48°N, 9.18°E– 16.16°E)	medBFM	0.71(±0.9)	0.06(±0.06)	-
	BGC-WMED	1.09(±1.3)	0.07(±0.04)	1.69(±0.8)
	WOA18	0.98(±0.8)	0.13(±0.02)	2.13(±0.4)
<i>DT3- Tyrrhenian South</i> (38°N– 39.18°N, 10°E– 16.16°E)	medBFM	0.68(±0.96)	0.06(±0.06)	-
	BGC-WMED	1.23(±1.5)	0.05(±0.05)	1.40(±0.9)
	WOA18	0.84(±0.8)	0.10(±0.01)	1.90(±0.2)
<i>DII- Sardinia Channel</i> (36°N– 39.18°N, 8.24°E– 10°E)	medBFM	0.62(±0.9)	0.05(±0.06)	-
	BGC-WMED	0.78(±1.3)	0.09(±0.06)	1.74(±0.9)
	WOA18	1.22(±0.8)	0.10(±0.007)	2.3(±0.30)
<i>DI3- Sicily Channel</i> (35°N– 38°N, 10°E–15°E)	medBFM	0.36(±0.5)	0.04(±0.03)	-
	BGC-WMED	1.04(±1.2)	0.13(±0.08)	2.15(±1.1)
	WOA18	0.72(±0.6)	0.08(±0.01)	1.79(±0.3)

603 4.3.3 Regional vertical comparison of nitrate and phosphate concentrations

604 As the last step in the comparison between the different products, it is investigated how the new
 605 climatology represents the vertical distribution by comparing the new climatological values for the
 606 period 2005-2017 with the medBFM reanalysis and the WOA18.

607 We extracted data values along a longitudinal transect across the Algerian basin in the west-east
 608 direction (Fig. 15). The transect was selected according to previous studies (D’Ortenzio and Ribera



609 d'Alcalà, 2009; Lazzari et al., 2012; Reale et al., 2020) and since the Easternmost part of the domain is
610 showing markedly features, a transect across the Tyrrhenian Sea is extracted as well (Fig. 15). Silicate
611 is not included as it was not represented in the medBFM model.

612 Vertical sections of nitrate and phosphate in the Algerian Sea show a common agreement between
613 products about the main patterns found along the water column, i.e. the nutrient depleted surface layer
614 and the gradual increase toward intermediate depths, we note as well the west to east decreasing gradient
615 in the three products, yet, there are some inequalities.

616 Below 100 m, there is a significant difference between products and a poor qualitative agreement.
617 Nitrate distribution is dominated by the nutrient enriched IW, with high values ($>7 \mu\text{mol kg}^{-1}$) increasing
618 from east to west (Fig. 15). Phosphate shows similar patterns in the surface layer, exhibiting very low
619 concentration in the surface layer and a progressive increase down to 300 m ($> 0.35 \mu\text{mol kg}^{-1}$) noted
620 also in the WOA18. The reanalysis showed a more smoothed field, below 100-300 m, with phosphate
621 concentration between 0.20 and $0.30 \mu\text{mol kg}^{-1}$. The highest values for phosphate were found below 250
622 m from 0°E to 3°E in the new product. The BCG-WMED transect define very well the different depth
623 layers, the upper intermediate layer is rich with nutrient concentration with $> 8 \mu\text{mol kg}^{-1}$ for nitrate
624 (BGC-WMED) and $>0.35 \mu\text{mol kg}^{-1}$ for phosphate (BGC-WMED and WOA18).

625 The vertical section along the Tyrrhenian Sea (Fig. 15) also shows a decrease from west to east in nitrate
626 concentrations. The same gradient is found also in phosphate in agreement with nutrient distribution
627 shown from the WOA18. From the section of the medBFM reanalysis, it is not easy to identify the west-
628 east gradient that we mentioned before. It could be suggested that the model under-estimate the vertical
629 features in the Eastern (Tyrrhenian Sea: 100-300 m, nitrate vary between 1.4 and $4.2 \mu\text{mol kg}^{-1}$,
630 phosphate between 0.13 and $0.20 \mu\text{mol kg}^{-1}$) and western part (Algerian basin: 100-300 m, nitrate vary
631 between 2.1 and $5.4 \mu\text{mol kg}^{-1}$, phosphate between 0.15 and $0.255 \mu\text{mol kg}^{-1}$). These values are lower
632 than the ones found in the BGC-WMED (Tyrrhenian Sea: 100-300 m, nitrate range between 3 to $6 \mu\text{mol}$
633 kg^{-1} , as for phosphate values oscillate between 0.10- $0.27 \mu\text{mol kg}^{-1}$; Algerian basin: 100-300 m, nitrate
634 range between 3.6 to $8 \mu\text{mol kg}^{-1}$, as for phosphate values oscillate between 0.18- $0.36 \mu\text{mol kg}^{-1}$).

635 While the WOA18 reproduce similar patterns as the new climatology (Tyrrhenian Sea: 100-300 m,
636 nitrate vary between 1.8 and $5.7 \mu\text{mol kg}^{-1}$, phosphate between 0.33 and $0.20 \mu\text{mol kg}^{-1}$) and western
637 part (Algerian basin: 100-300 m, nitrate vary between 2.8 and $6.8 \mu\text{mol kg}^{-1}$, phosphate between 0.16
638 and $0.34 \mu\text{mol kg}^{-1}$).

639 The products illustrate the nutrient-poor water in the eastern side (Tyrrhenian Sea) and the relatively
640 nutrient-rich water found in the western transect (Algerian basin).



641 The BGC-WMED product capture details in Fig. 15 about the longitudinal gradient in nitrate and
642 phosphate, along the water column where nutrient sink deeper from west to east as previously seen in
643 Pujo-Pay et al. (2011) and Krom et al. (2014), an increased oligotrophy from west to east with higher
644 concentrations in the two nutrients in the western side of the section and a more oligotrophic character
645 toward east.

646 The differences between products could be explained by the difference in the data coverage, time span
647 and the difference in methods used to construct the climatological fields.

648 The variability in nitrate and phosphate fields along the transect extracted from the BGC-WMED reflects
649 the high resolution of the product allowing the screening of vertical structure controlling nutrient
650 contents. Based on a visual comparison, the new product is able to reproduce similar patterns as to the
651 WOA18 and to a lesser extend the medBFM reanalysis.

652 Fig. 16 examines the vertical difference of nitrate and phosphate concentration for the BGC-WMED
653 with the medBFM reanalysis along the Algerian basin (Fig.16a, nitrate; Fig.16b, phosphate) and
654 WOA18 (Fig.16c, nitrate; Fig.16d, phosphate).

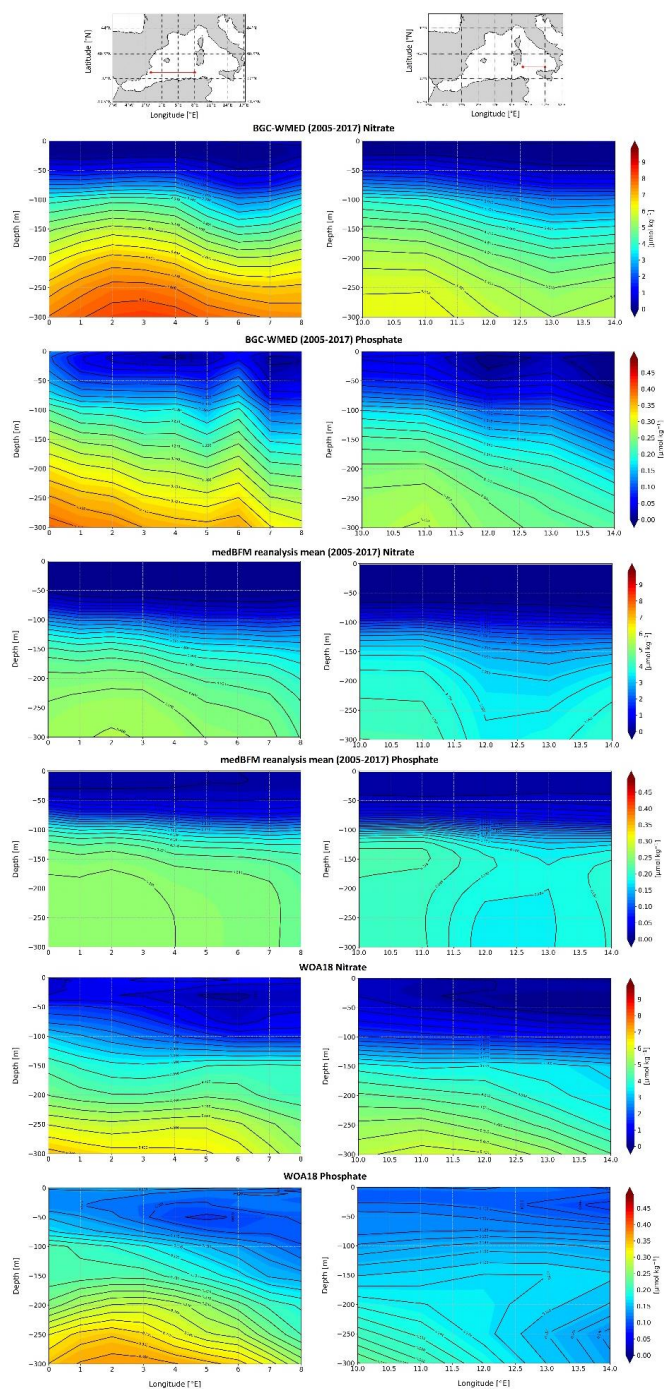
655 The vertical section shows a strong agreement at the surface for nitrate between the BGC-WMED and
656 the medBFM reanalysis (Fig. 16a), while the vertical difference with WOA18 demonstrates that nitrate
657 values in the new product are lower than the WOA18 at 50- 75 m (Fig. 16c).

658 The difference increases with depth, below 100 m, the BGC-WMED nitrate climatology is higher than
659 the medBFM with a difference ranging between 0.6 and 2.4 $\mu\text{mol kg}^{-1}$, similar observation is noted in
660 the WOA18 (Fig. 16c). In Fig.16a and Fig.16c, we identify patterns in the vertical structure of nitrate
661 in the eaten portion of the transect.

662 Regarding phosphate, differences between the new climatology and the medBFM reanalysis are noted
663 (Fig. 16b) where the BGC-WMED show high concentrations in the first 100 m and between 150 m and
664 300 m (differences of 0.02 - 0.08 $\mu\text{mol kg}^{-1}$), this difference decreases at 100-150 m. At the eastern
665 portion of the transect (6°E to 7.5°E), we find an agreement between the two products.

666 Conversely, the vertical sections of the differences between BGC-WMED and WOA18 in phosphate
667 (Fig.16 d) show similarities, with the new product being lower than the WOA18 in the first 50 m. Large
668 difference is found on both sides of the transect below 100 m, while in the center of the transect, the
669 difference in phosphate is reduced to 0-0.02 $\mu\text{mol kg}^{-1}$.

670 Fig.17 compares the vertical difference of nitrate and phosphate along the Tyrrhenian Sea transect. In
671 general, the difference transect in the Tyrrhenian Sea shows similar features with medBFM reanalysis
672 and the WOA18 as in Algerian basin. Fig.17d captures the west to east gradient in phosphate. The
673 WOA18 overestimate phosphate in the surface layer.



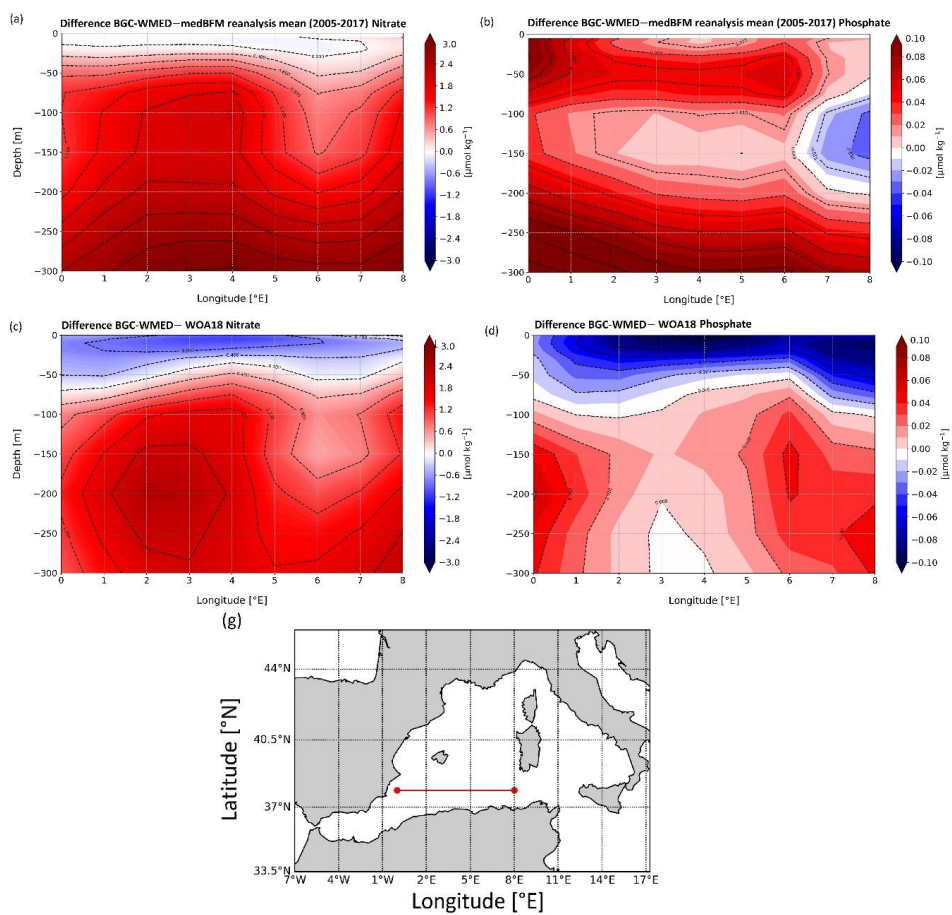


675 **Figure 15.** Vertical distribution of nitrate and phosphate from the Algerian basin and Tyrrhenian Sea.
676 Colors show the gridded values from the three different products: BGC-WMED, medBFM reanalysis
677 (Teruzzi et al.,2019) and the WOA18 (Garcia et al., 2019).



678 Based on the new climatology comparison with the WOA18 and the reanalysis, it is concluded that the
679 new product is consistent with the main features of previous products and show the large-scale patterns
680 and underline well the characteristics of the water mass layers.

681 The study also provides an examination of the nitrate and phosphate distributions along a longitudinal
682 transect across the Algerian Basin (Western WMED) and across the Tyrrhenian Sea (Eastern WMED).
683 We have shown that the western basin is relatively high in nutrient compared to the Eastern basin. The
684 increased oligotrophic gradient from west to east could be attributed to the difference in the
685 hydrodynamic patterns related to the water mass specific properties that are affected by the EMED and
686 the Atlantic ocean inflows, and to the local sources of nutrients (Ribera d'Alcalà et al., 2003; Schroeder
687 et al., 2010). Study of Crispi et al. (2001) inferred to the biological activity that is responsible for the
688 oligotrophic gradient.

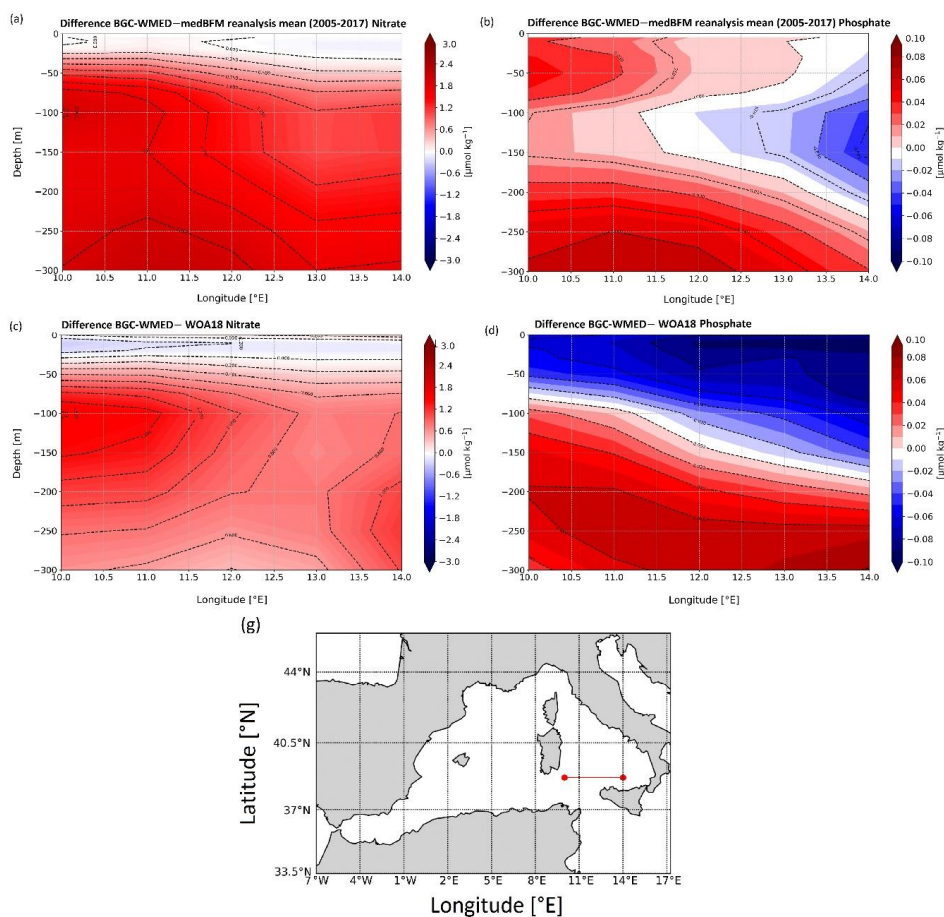


689

690 **Figure 16.** Difference of vertical section from the Algerian basin between BGC-WMED and medBFM

691 (a. nitrate, b. phosphate), BGC-WMED and WOA18 (c. nitrate, d. phosphate), with dashed contour lines

692 and labels.



693

694 **Figure 17.** Same as Fig.16 but for the vertical section from the Tyrrhenian Sea.

695 4.4 Temporal comparison: 1981-2004 vs 2005-2017

696 In this section, we compare between two climatological periods (1981-2004 vs 2005-2017). The
697 distinction between the two period was based on the occurrence of the western Mediterranean transition
698 (WMT) that started in 2004/05, during which there was a progressive increase in temperature and
699 salinity of the IW that led to important deep convection events, substantially increasing the rate of DW
700 formation between 2004 and 2005 (Schroeder et al., 2016).

701 The result of this climatological event was that a newly generated DW, denser, saltier, and warmer than
702 the old WMDW, filled up the WMED. The new WMDW propagated east toward the Tyrrhenian Sea
703 and west toward the Alboran Sea and Gibraltar (Schroeder et al., 2016).

704 A recent study of Li and Tanhua (2020) demonstrated an enhanced ventilation in the WMED deep layers
705 despite the continuous overall increase in temperature (Bindoff et al., 2007), salinity and density of



706 intermediate and deep layers after the WMT (Schroeder et al., 2016; Vargas-Yáñez, 2017). An increased
707 ventilation means a DW renewal (Schroeder et al., 2016; Tanhua et al., 2013) subsequently a well
708 oxygenated waters, implying an increase in the decomposition of the sinking organic matters into
709 inorganic nutrients, thus causing changes of biogeochemical cycles (Shepherd et al., 2017). What
710 happened in the WMED was not a permanent continuous event, since DW formation faded during the
711 years 2006 and 2007, to restart again in 2008 (Li and Tanhua, 2020). In this section, we investigate the
712 possible impact of WMT on biogeochemical characteristics at different depth levels (with a focus on
713 nitrate, phosphate and silicate regional distribution and patterns).

714 We considered depth levels that represent the usual three layers: the surface (100 m; Fig.18a-19a-20a),
715 intermediate (300 m; Fig.18b-19b-20b) and deep layers (1500 m; Fig.18c-19c-20c).

716 The WMED surface layer is dominated by the AW coming through the Alboran Sea, a permanent area
717 of upwelling (García-Martínez et al., 2019), where there is a continuous input of elements from the layer
718 below to the surface (Fig. 18a-19a-20a). Nitrate increased after WMT (Fig. 18d-19d-20d) by $+0.4137$
719 $\mu\text{mol kg}^{-1}$ (Fig.1Sa). The largest difference between the two periods reached $>+2 \mu\text{mol kg}^{-1}$ in Sardinia
720 Channel and the Alboran Sea that was explained by the favorable conditions for nitrogen fixation as
721 discussed in Rahav et al. (2013), revealing also that nitrogen fixation rate increased from east-to-west.
722 Phosphate and silicate on the other hand described a decrease at 100 m (Fig. A1a) with about -0.021 and
723 $-0.1365 \mu\text{mol kg}^{-1}$ in average, respectively. Large change is noticed in the southern Alboran Sea, Sardinia
724 channel and Balearic Sea.

725 The surface layer exhibits an irregular distribution since it is subjected to seasonal variability. We found
726 and increase in all nutrients at 300 and 1500 m with a maximum identified at intermediate depth in both
727 nitrate and phosphate which is explained by the remineralization of organic matter along the path of the
728 IW. The latter flows westward (from the Levantine to the Atlantic Ocean). Its content in nutrients
729 increases (relatively to the conditions in the EMED) with age (Schroeder et al., 2020). It arrives to the
730 Tyrrhenian Sea, where in Fig.18b-19b-20b (at 300 m depth), we identify a nutrient-depleted intermediate
731 layer. At this depth level, we observe a gain in the three nutrients after WMT (Fig.18e-19e-20e). In
732 average, the difference between the two periods (pre/post-WMT) for nitrate, phosphate, and silicate, is
733 around $+0.8648$, $+0.0068$ and $+0.2072 \mu\text{mol kg}^{-1}$ (Fig. A1b), respectively.

734 A similar increase after WMT in the deep layer (1500 m), is also found for nutrient concentrations (Fig.
735 18f, 19f, 20f) in the magnitude of $+0.753$ for nitrate, $+0.025$ for phosphate, and $+0.867$ for silicate (Fig.
736 A1c), which highlights an increase in the downward flow of organic matter remineralization that is
737 supplying the existing pool.

738

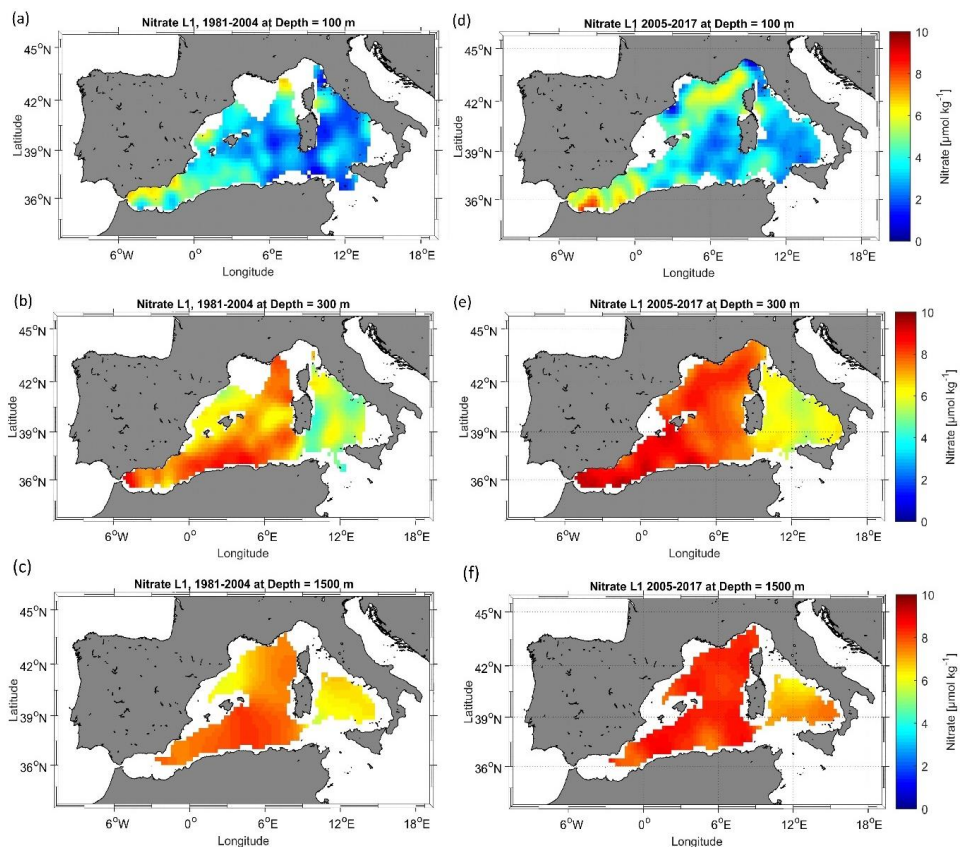
739 This increase is also illustrated in the climatological mean vertical profile of Fig. 21 in the three nutrients.
740 Nitrate displays a notable vertical difference to the pre-WMT period below 200 m (Fig.21a). Phosphate
741 difference between the two-time period is larger below 400 m (Fig. 21b). Silicate was different than



742 nitrate and phosphate. It increases progressively with depth (Fig.20c) and demonstrated an enrichment
743 of the DW compared to the 1981-2004 period (Fig. 21c). The maximum values are found in the deep
744 layer, due to the low remineralization rate. With the warming climate, biogenic silicate tends to dissolve
745 faster which explain the high concentrations all over the basin even the Tyrrhenian Sea after the WMT.
746 According to Stöven and Tanhua (2014), the impressive volume of the newly formed DW during 2004
747 and 2006, ventilated the old DW decreasing its age, meaning that the WMT could have led to the
748 lowering of the WMED deep layer pool in nutrient as it was pointed out by Schroeder et al. (2010).
749 However, we did not observe this decrease in the climatological analysis after the WMT. It might be
750 due to the temporal variability of the deep convection intensity, since a decrease has been recorded in
751 the Gulf of Lion between 2007 and 2013 (Houpert et al., 2016).

752 A decrease in the deep convection intensity since the WMT (Houpert et al., 2016; Li and Tanhua, 2020),
753 could potentially lead to the reduction in the supply from the nutrient-rich DW (before WMT) to the
754 surface, i.e. the decrease in nutrient could have happened right after the WMT in spring 2005 where
755 Schroeder et al. (2010) reported peculiar divergence between the old WMDW and the new WMDW in
756 nitrate and phosphate; the new WMDW was low in nutrient; later on an intense DW formation event
757 marked the year 2012 with a strong ventilation that has been recorded in the Adriatic Sea that could
758 have affected the WMED. It was not possible to observe this change since we calculated the mean state
759 of the basin spanning specific period.

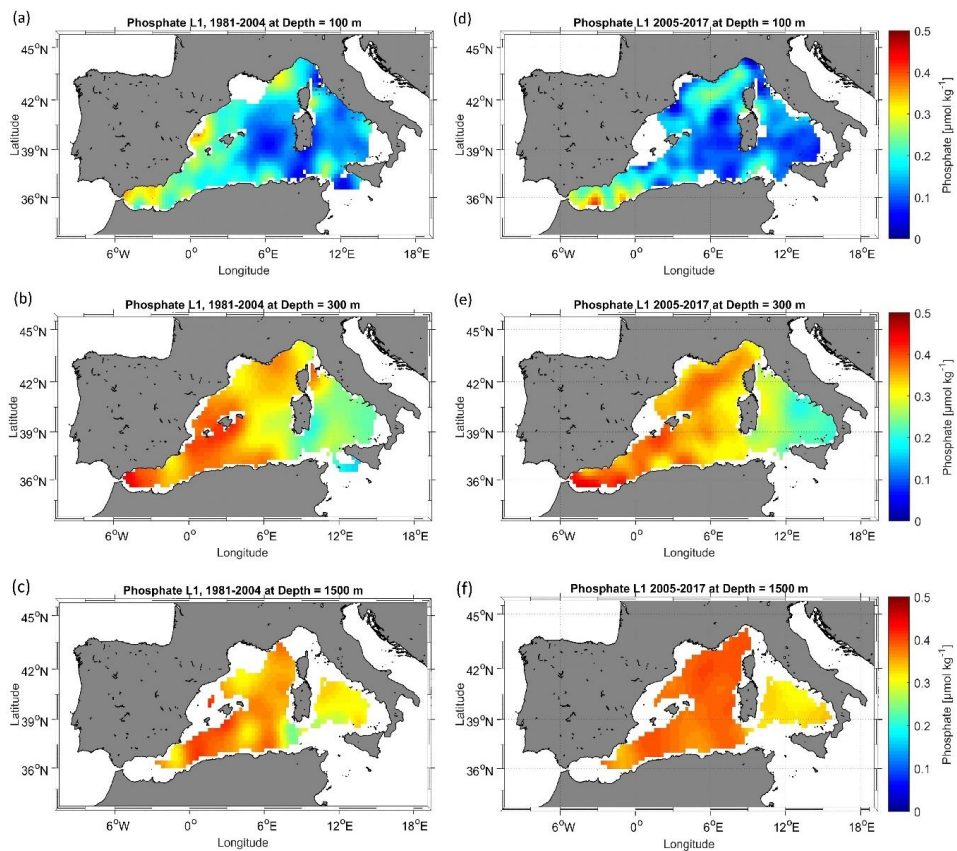
760 The spatial distribution of nutrient concentrations after the WMT (2005-2017) was quite different from
761 the one before the WMT (1981-2004). This could also be related to the significant decline in river
762 discharge between 1960 and 2000, that was estimated to 20% (Ludwig et al., 2009). The change could
763 be explained by the low denitrification rate for nitrate and an increase in the remineralization of organic
764 matter, loading the deep layer with inorganic nutrients, also it could be associated with the slower
765 ventilation of the WMED waters and a longer residence time.



766

767 **Figure 18.** Nitrate climatological field (masked analysis fields masked using relative error threshold =

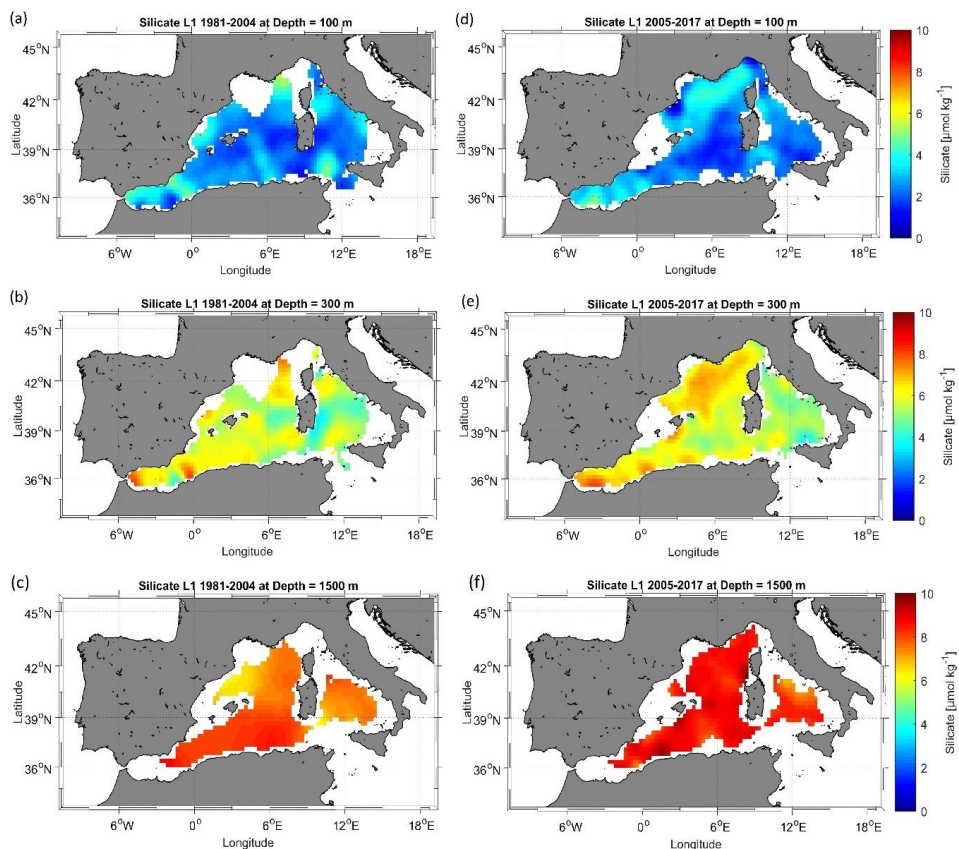
768 0.3 (L1)) at 100 m, 300 m, and 1500 m, for two periods: 1981-2004 (a, b, c) and 2005-2017 (d, e, f).



769

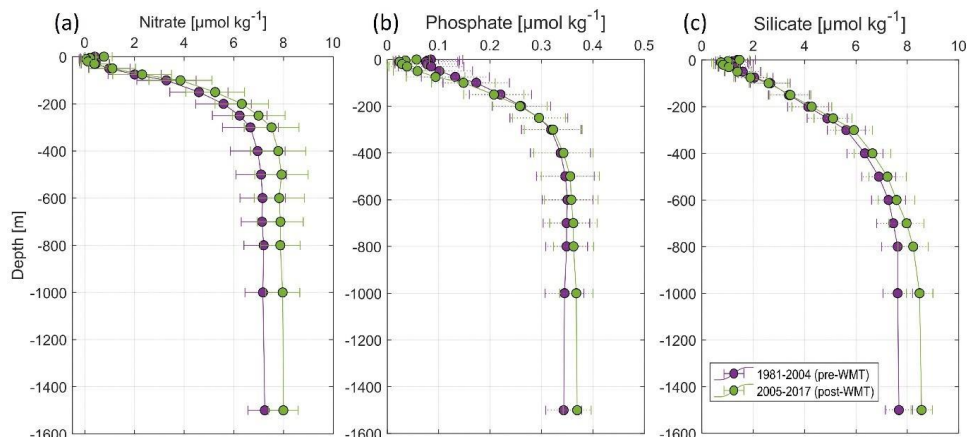
770 **Figure 19.**The same as Fig. 18 but for phosphate.

771



772

773 **Figure 20.** The same as Fig. 18 but for silicate.



774

775 **Figure 21.** Climatological mean vertical profile and standard deviation of (a) nitrate, (b) phosphate and
 776 (c) silicate over the WMED before (1981-2004, in violet) and after WMT (2005-2017, in green).



777 **5 Data availability**

778 The final product is available as netCDF files from PANGAEA and can be accessed at
779 <https://doi.pangaea.de/10.1594/PANGAEA.930447> (Belgacem et al., 2021, DOI registration in
780 progress). Ancillary information is in the readme in PANGAEA with the list of variables that is
781 described in table 3 of section 4.

782 **6 Conclusion**

783 In this study, we investigated spatial variability of the inorganic nutrients in the WMED and present a
784 climatological field reconstruction of nitrate, phosphate, and silicate, using an important collection
785 dataset spanning 1981 and 2017. The BGC-WMED new product is generated on 19 vertical levels on
786 $1/4^\circ$ spatial resolution grid.

787 The new product represents very well spatial patterns about nutrient distribution because of its higher
788 spatial and temporal data coverage compared to the existing climatological products (see Table 1), it is
789 contributing to the understanding of the spatial variability of nutrients in the WMED.

790 The novelty of the present work is the use of the variational analysis that takes into consideration
791 physical, geographical boundaries and topography, the resulting estimate of associated error field.

792 Comparison with previously reported studies gives that the BGC-WMED reproduces common features
793 and agrees with previous records. The reference products WOA18 and medBFM biogeochemical
794 reanalysis tend to underestimate nutrient distribution in the region with respect to the new product.

795 The new product captures the strong east-west gradient of and vertical features. The results obtained do
796 not include seasonal or annual analysis fields. However, the aggregated dataset here does show
797 improvements in describing the spatial distribution of inorganic nutrients in the WMED. We
798 acknowledge that computing a climatological mean over a time period is not enough to estimate and
799 detect the climate shift ‘WMT’ change driven trend. However, comparing climatologies based on the
800 two time periods: 1981-2004 (pre-WMT) and 2005 -2017 (post-WMT) has already produced important
801 results. Notable changes have been found in nutrient distribution after the WMT at various depths.

802 The results support the tendency to a relative increasing load of inorganic nutrients to the WMED and
803 possibly relate the change in general circulation patterns, changes in deep stratification and warming
804 trends, however, this remains to be evidenced.

805 The BGC-WMED is a regional climatology that has allowed the identification of a substantial
806 enrichment of the waters, except for the Tyrrhenian Sea where the water column is depleted in nutrients
807 with respect to the western areas of the WMED. The climatology gave information about the spreading
808 of inorganic nutrients inside the WMED at surface, intermediate and deep layers.



809 A future work will suggest a better understanding of the change in nutrients related to water masses
810 associated with ventilation rate, a climatological field along isopycnal surfaces instead of depths and the
811 correlation between potential temperature and nutrients.

812 **Author contributions**

813 The BGC-WMED climatology product was led between the CNR-ISMAR and DAIS- University of
814 Venice. MB, KS and JC designed the experiment and contributed to the writing of the manuscript. AB
815 and CT helped MB to perform the analysis and contributed to the manuscript. BP contributed to
816 specific parts of the manuscript.

817 **Acknowledgements**

818 Data was provided through SeaDataNet Pan-European infrastructure for ocean and marine data
819 management (<https://www.seadatanet.org>), Mediterranean Ocean Observing System for the
820 Environment, MOOSE (<http://www.moose-network.fr/>). MB acknowledge the WOA18 and CMEMS
821 for the medBFM data (<https://help-cmems.mercator-ocean.fr/en/articles/4444611-how-to-cite-or-reference-copernicus-marine-products-and-services>). We wish to thank all colleagues who contributed
822 in the data acquisition, and the PIs if the cruises involved. MB thanks Kanwal Shahzadi from the
823 university of Bologna for the discussions during our internship at GHER, university of Liege. JC and
824 KS acknowledge several of national and European projects, e.g.: KM3NeT, EU GA #011937; SESAME,
825 EU GA #GOCE-036949; PERSEUS, EU GA #287600; OCEAN-CERTAIN, EU GA #603773;
826 COMMON SENSE, EU GA #228344; EUROFLEETS, EU GA #228344; EUROFLEETS2, EU GA #
827 312762; JERICO, EU GA #262584; the Italian PRIN 2007 program “Tyrrhenian Seamounts
828 ecosystems”, and the Italian RITMARE Flagship Project, both funded by the Italian Ministry of
829 University and Research.

831 **References**

- 832 Barnes, S.L. (1964). A technique for maximizing details in numerical weather map analysis. *J. App.*
833 *Meteor.*, 3, 396-409.
- 834 Barnes, S.L. (1994). Applications of the Barnes Objective Analysis Scheme, Part III: Tuning for
835 Minimum Error. *J. Atmosph. and Oceanic Tech.*, 11, 1459-1479.
- 836 Barth, A., Troupin, C., Alvera-Azcárate, A. and Vandenbulcke, L.: Divand-1.0: N-dimensional
837 variational data analysis for ocean observations, *Geosci. Model Dev.*, 7(1), 225–241,
838 <https://doi.org/10.5194/gmd-7-225-2014>, 2014.
- 839 Beckers, J. M., Barth, A., Troupin, C. and Alvera-Azcárate, A.: Approximate and efficient methods to
840 assess error fields in spatial gridding with data interpolating variational analysis (DIVA), *J. Atmos.*
841 *Ocean. Technol.*, 31(2), 515–530, <https://doi.org/10.1175/JTECH-D-13-00130.1>, 2014.
- 842 Belgacem, M., Chiggiato, J., Borghini, M., Pavoni, B., Cerrati, G., Aciri, F., Cozzi, S., Ribotti, A.,
843 Álvarez, M., Lauvset, S. K., Schroeder, K. : Quality controlled dataset of dissolved inorganic nutrients



- 844 in the western Mediterranean Sea (2004-2017) from R/V oceanographic
845 cruises. PANGAEA, <https://doi.org/10.1594/PANGAEA.904172>, 2019
- 846 Belgacem, M., Chiggiato, J., Borghini, M., Pavoni, B., Cerrati, G., Aciri, F., Cozzi, S., Ribotti, A.,
847 Álvarez, M., Lauvset, S. K. and Schroeder, K.: Dissolved inorganic nutrients in the western
848 Mediterranean Sea (2004-2017), *Earth Syst. Sci. Data*, 12(3), 1985–2011, [https://doi.org/10.5194/essd-](https://doi.org/10.5194/essd-12-1985-2020)
849 12-1985-2020, 2020.
- 850 Belgacem, M., Schroeder, K., Barth, A., Troupin, C., Pavoni, B., Chiggiato, J. : A climatological
851 product of inorganic nutrient distributions on the Western Mediterranean Sea (BGC-WMED) derived
852 from cruise-based measurements spanning 1981 to
853 2017. PANGAEA, <https://doi.pangaea.de/10.1594/PANGAEA.930447> (DOI registration in progress),
854 2021.
- 855 Bethoux, J. P., Morin, P., Madec, C. and Gentili, B.: Phosphorus and nitrogen behaviour in the
856 Mediterranean Sea, *Deep Sea Res. Part A, Oceanogr. Res. Pap.*, 39(9), 1641–1654,
857 [https://doi.org/10.1016/0198-0149\(92\)90053-V](https://doi.org/10.1016/0198-0149(92)90053-V), 1992.
- 858 Brankart, J. M. and Brasseur, P.: The general circulation in the Mediterranean Sea: A climatological
859 approach, *J. Mar. Syst.*, 18(1–3), 41–70, [https://doi.org/10.1016/S0924-7963\(98\)00005-0](https://doi.org/10.1016/S0924-7963(98)00005-0), 1998.
- 860 Brasseur, P. & Haus, J.: Application of a 3-D variational inverse model to the analysis of
861 ecohydrodynamic data in the Northern Bering and Southern Chukchi Seas. *Journal of Marine Systems*,
862 1: 383_401. [https://doi.org/10.1016/0924-7963\(91\)90006-G](https://doi.org/10.1016/0924-7963(91)90006-G), 1991.
863
- 864 Bindoff, N.L., Willebrand, J., Artale, V., Cazenave, A., Gregory, J., Gulev, S., Hanawa, K., Le Quéré,
865 C., Levitus, S., Nojiri, Y., Shum, C.K., Talley, L.D. and Unnikrishnan, A.: Observations: Oceanic
866 Climate Change and Sea Level. In: *Climate Change 2007: The Physical Science Basis. Contribution of*
867 *Working Group I to the Fourth Assessment Report of the Intergovernmental Panel on Climate Change*
868 *[Solomon, S., D. Qin, M. Manning, Z. Chen, M. Marquis, K.B. Averyt, M. Tignor and H.L. Miller*
869 *(eds.)]. Cambridge University Press, Cambridge, United Kingdom and New York, NY, USA, 2007.*
- 870 Brasseur, P., Beckers, J. M., Brankart, J. M. and Schoenauen, R.: Seasonal temperature and salinity
871 fields in the Mediterranean Sea: Climatological analyses of a historical data set, *Deep. Res. Part I*
872 *Oceanogr. Res. Pap.*, 43(2), 159–192, [https://doi.org/10.1016/0967-0637\(96\)00012-X](https://doi.org/10.1016/0967-0637(96)00012-X), 1996.
- 873 Brasseur, P. P.: A variational inverse method for the reconstruction of general circulation fields in the
874 northern Bering Sea, *J. Geophys. Res.*, 96(C3), 4891, <https://doi.org/10.1029/90jc02387>, 1991.
- 875 Buga, L., Eilola, K., Wesslander, K., Fryberg, L., Gatti, J., Leroy, D., Iona, S., Tsompanou, M. and
876 Lipizer, M.: EMODnet Thematic Lot n ° 4 / SI2 . 749773 Interpolating Variational Analysis (DIVA).
877 Release 2018, , <https://doi.org/10.6092/A8CFB472-10DB-4225-9737-5A60DA9AF523>, 2019.
- 878 L. Buga, G. Sarbu, K. Eilola, K. Wesslander, L. Fryberg, W. Magnus, J. Gatti, D. Leroy, S. Iona, M.
879 Tsompanou, P. Karagevrekis, Jonas Koefoed Rømer, Larsen, J. Koefoed Rømer, A.K. Østrem, M.
880 Lipizer, A. Giorgetti. 2019 EMODnet Chemistry Regional climatologies produced with Data-
881 Interpolating Variational Analysis (DIVA). Release 2018. [https://doi.org/10.6092/A8CFB472-10DB-](https://doi.org/10.6092/A8CFB472-10DB-4225-9737-5A60DA9AF523)
882 4225-9737-5A60DA9AF523
- 883 Conkright, M. E., BOYER, T. P., and Levitus, S.: Quality control and processing of historical
884 oceanographic nutrient data. US Department of Commerce, National Oceanic and Atmospheric
885 Administration, National Environmental Satellite, Data, and Information Service, 1994.
- 886 Cressman, G., An operational objective analysis system, *MWR*, 1959, 88, 327--342, [https://doi.org/](https://doi.org/10.1175/1520-0493(1959)087<0367:AOOAS>2.0.CO;2)
887 10.1175/1520-0493(1959)087<0367:AOOAS>2.0.CO;2, 1959.
- 888 Crispi, G., Mosetti, R., Solidoro, C. and Crise, A.: Nutrients cycling in Mediterranean basins: The role
889 of the biological pump in the trophic regime, in *Ecological Modelling*, vol. 138, pp. 101–114., 2001.
- 890 Crombet, Y., Leblanc, K., Quéuiner, B., Moutin, T., Rimmelin, P., Ras, J., Claustre, H., Leblond, N.,



- 891 Oriol, L. and Pujo-Pay, M.: Deep silicon maxima in the stratified oligotrophic Mediterranean Sea,
892 Biogeosciences, 8(2), 459–475, <https://doi.org/10.5194/bg-8-459-2011>, 2011.
- 893 D’Ortenzio, F. and Ribera d’Alcalà, M.: On the trophic regimes of the Mediterranean Sea: a satellite
894 analysis, Biogeosciences Discuss., 5(4), 2959–2983, <https://doi.org/10.5194/bgd-5-2959-2008>, 2009.
- 895 D’Ortenzio, F., Taillandier, V., Claustre, H., Prieur, L. M., Leymarie, E., Mignot, A., Poteau, A.,
896 Penker, C. and Schmechtig, C. M.: Biogeochemical Argo : The Test Case of the NAOS Mediterranean
897 Array, , 7(March), 1–16, <https://doi.org/10.3389/fmars.2020.00120>, 2020.
- 898 DeMaster, D. J.: The accumulation and cycling of biogenic silica in the Southern Ocean: Revisiting the
899 marine silica budget, Deep. Res. Part II Top. Stud. Oceanogr., 49(16), 3155–3167,
900 [https://doi.org/10.1016/S0967-0645\(02\)00076-0](https://doi.org/10.1016/S0967-0645(02)00076-0), 2002.
- 901 Desroziers, G., Berre, L., Chapnik, B. and Poli, P.: Diagnosis of observation, background and analysis-
902 error statistics in observation space, Q. J. R. Meteorol. Soc., 131(613), 3385–
903 3396, <https://doi.org/10.1256/qj.05.108>, 2005.
- 904 Diaz, P., Raimbault, F., Boudjellal, B., Garcia, N. and Moutin, T.: Early spring phosphorus limitation
905 of primary productivity in a NW Mediterranean coastal zone (Gulf of Lions), Mar. Ecol. Prog. Ser.,
906 211(McGill 1965), 51–62, <https://doi.org/10.3354/meps211051>, 2001.
- 907 Fichaut, M., Garcia, M. J., Giorgetti, A., Iona, A., Kuznetsov, A., Rixen, M. and Group, M.:
908 MEDAR/MEDATLAS 2002: A Mediterranean and Black Sea database for operational oceanography,
909 Elsevier Oceanogr. Ser., 69(C), 645–648, [https://doi.org/10.1016/S0422-9894\(03\)80107-1](https://doi.org/10.1016/S0422-9894(03)80107-1), 2003.
- 910 de Fommervault, O. P., Migon, C., D’Ortenzio, F., Ribera d’Alcalà, M. and Coppola, L.: Temporal
911 variability of nutrient concentrations in the northwestern Mediterranean sea (DYFAMED time-series
912 station), Deep. Res. Part I Oceanogr. Res. Pap., 100, 1–12, <https://doi.org/10.1016/j.dsr.2015.02.006>,
913 2015.
- 914 Frings, P. J., Clymans, W., Fontorbe, G., De La Rocha, C. L. and Conley, D. J.: The continental Si cycle
915 and its impact on the ocean Si isotope budget, Chem. Geol., 425, 12–36,
916 <https://doi.org/10.1016/j.chemgeo.2016.01.020>, 2016.
- 917 Gacic, M., Civitarese, G., Kovacevic, V., Ursella, L., Bensi, M., Menna, M., et al. : Extreme winter 2012
918 in the Adriatic: an example of climatic effect on the BiOS rhythm. Ocean Sci. 10, 513–
919 522. <https://doi.org/10.5194/os-10-513-2014>, 2014.
- 920 García-Martínez, M. del C., Vargas-Yáñez, M., Moya, F., Santiago, R., Muñoz, M., Reul, A., Ramírez,
921 T. and Balbín, R.: Average nutrient and chlorophyll distributions in the western Mediterranean:
922 RADMED project, Oceanologia, 61(1), 143–169, <https://doi.org/10.1016/j.oceano.2018.08.003>, 2019.
- 923 Garcia, H. E., Weathers, K. W., Paver, C. R., Smolyar, I., Boyer, T. P., Locarnini, R. A., Zweng, M. M.,
924 Mishonov, A. V., Baranova, O. K., Seidov, D. and Reagan, J. R.: World Ocean Atlas 2018. Vol. 4:
925 Dissolved Inorganic Nutrients (phosphate, nitrate and nitrate+nitrite, silicate). A. Mishonov Technical
926 Editor, NOAA Atlas NESDIS 84, 35pp, 2019. Giorgi, F.: Climate change hot-spots, Geophys. Res. Lett.,
927 33(8), 1–4, <https://doi.org/10.1029/2006GL025734>, 2006.
- 928 Hecht, A., Pinardi, N. and Robinson, A. R.: Currents, Water Masses, Eddies and Jets in the
929 Mediterranean Levantine Basin, J. Phys. Oceanogr., 18(10), 1320–1353, 1988.
- 930 Houpert, L., Durrieu de Madron, X., Testor, P., Bosse, A., D’Ortenzio, F., Bouin, M. N., Dausse, D., Le
931 Goff, H., Kunesch, S., Labaste, M., Coppola, L., Mortier, L. and Raimbault, P.: Observations of open-
932 ocean deep convection in the northwestern Mediterranean Sea: Seasonal and interannual variability of
933 mixing and deep water masses for the 2007-2013 Period, J. Geophys. Res. Ocean., 121(11), 8139–
934 8171, <https://doi.org/10.1002/2016JC011857>, 2016.
- 935 Iona, A., Theodorou, A., Watelet, S., Troupin, C., Beckers, J.-M., and Simoncelli, S.: Mediterranean
936 Sea Hydrographic Atlas: towards optimal data analysis by including time-dependent statistical



- 937 parameters, *Earth Syst. Sci. Data*, 10, 1281–1300, <https://doi.org/10.5194/essd-10-1281-2018>, 2018.
- 938 Key, R. M., Kozyr, A., Sabine, C. L., Lee, K., Wanninkhof, R., Bullister, J. L., Feely, R. A., Millero, F.
939 J., Mordy, C. and Peng, T. H.: A global ocean carbon climatology: Results from Global Data Analysis
940 Project (GLODAP), *Global Biogeochem. Cycles*, 18(4), 1–23, <https://doi.org/10.1029/2004GB002247>,
941 2004.
- 942 Krom, M. D., Oceanographic, I. and Shikmona, T.: Nutrient budget for the Eastern Mediterranean :
943 Implications for phosphorus limitation, , 49(5), 1582–1592, 2004.
- 944 Krom, M. D., Emeis, K. C. and Van Cappellen, P.: Why is the Eastern Mediterranean phosphorus
945 limited?, *Prog. Oceanogr.*, 85(3–4), 236–244, <https://doi.org/10.1016/j.pocean.2010.03.003>, 2010.
- 946 Krom, M. D., Kress, N. and Fanning, K.: Silica cycling in the ultra-oligotrophic eastern Mediterranean
947 Sea, *Biogeosciences*, 11(15), 4211–4223, <https://doi.org/10.5194/bg-11-4211-2014>, 2014.
- 948 Lascaratos, A., Roether, W. and Nittis, K.: Recent changes in deep water formation and spreading in the
949 eastern Mediterranean Sea : a review, , 44, 5–36, 1999.
- 950 Lauvset, S. K., Key, R. M., Olsen, A., Van Heuven, S., Velo, A., Lin, X., Schirnack, C., Kozyr, A.,
951 Tanhua, T., Hoppema, M., Jutterström, S., Steinfeldt, R., Jeansson, E., Ishii, M., Perez, F. F., Suzuki, T.
952 and Watelet, S.: A new global interior ocean mapped climatology: The $1^\circ \times 1^\circ$ GLODAP version 2,
953 *Earth Syst. Sci. Data*, 8(2), 325–340, <https://doi.org/10.5194/essd-8-325-2016>, 2016.
- 954 Lavigne, H.: On the vertical distribution of the chlorophyll a concentration in the Mediterranean Sea : a
955 basin scale and seasonal approach, , (March), <https://doi.org/10.5194/bgd-12-4139-2015>, 2015.
- 956 Lazzari, P., Solidoro, C., Ibello, V., Salon, S., Teruzzi, A., Béranger, K., Colella, S. and Crise, A.:
957 Seasonal and inter-annual variability of plankton chlorophyll and primary production in the
958 Mediterranean Sea: A modelling approach, *Biogeosciences*, 9(1), 217–233, <https://doi.org/10.5194/bg-9-217-2012>, 2012.
- 960 Lazzari, P., Solidoro, C., Salon, S. and Bolzon, G.: Spatial variability of phosphate and nitrate in the
961 Mediterranean Sea: A modeling approach, *Deep. Res. Part I Oceanogr. Res. Pap.*, 108, 39–52,
962 <https://doi.org/10.1016/j.dsr.2015.12.006>, 2016.
- 963 Levitus, S.: Climatological Atlas of the World Ocean, *Eos, Trans. Am. Geophys. Union*, 64(49), 962–
964 963, <https://doi.org/10.1029/EO064i049p00962-02>, 1982.
- 965 Li, P. and Tanhua, T.: Recent Changes in Deep Ventilation of the Mediterranean Sea; Evidence From
966 Long-Term Transient Tracer Observations, *Front. Mar. Sci.*, 7(July), 1–23,
967 <https://doi.org/10.3389/fmars.2020.00594>, 2020.
- 968 Lipizer, M., Partescano, E., Rabitti, A., Giorgetti, A. and Crise, A.: Qualified temperature, salinity and
969 dissolved oxygen climatologies in a changing Adriatic Sea, *Ocean Sci.*, 10(5), 771–797,
970 <https://doi.org/10.5194/os-10-771-2014>, 2014.
- 971 Lucea, A., Duarte, C. M. and Agustí, S.: Nutrient (N , P and Si) and carbon partitioning in the stratified
972 NW Mediterranean, , 49, 157–170, [https://doi.org/10.1016/S1385-1101\(03\)00005-4](https://doi.org/10.1016/S1385-1101(03)00005-4), 2003.
- 973 Ludwig, W., Dumont, E., Meybeck, M. and Heussner, S.: River discharges of water and nutrients to the
974 Mediterranean and Black Sea: Major drivers for ecosystem changes during past and future decades?,
975 *Prog. Oceanogr.*, 80(3–4), 199–217, <https://doi.org/10.1016/j.pocean.2009.02.001>, 2009.
- 976 Ludwig, W., Bouwman, A. F., Dumont, E. and Lespinas, F.: Water and nutrient fluxes from major
977 Mediterranean and Black Sea rivers: Past and future trends and their implications for the basin-scale
978 budgets, *Global Biogeochem. Cycles*, 24(4), 1–14, <https://doi.org/10.1029/2009GB003594>, 2010.
- 979 Maillard, C., Lowry, R., Maudire, G. and Schaap, D.: SeaDataNet: Development of a Pan-European
980 infrastructure for ocean and marine data management, in *OCEANS 2007 - Europe.*, 2007.
- 981 Malanotte-Rizzoli, P., Manca, B. B., D’Alcala, M. R., Theocharis, A., Brenner, S., Budillon, G. and



- 982 Ozsoy, E.: The Eastern Mediterranean in the 80s and in the 90s: The big transition in the intermediate
983 and deep circulations, *Dyn. Atmos. Ocean.*, 29(2–4), 365–395, [https://doi.org/10.1016/S0377-](https://doi.org/10.1016/S0377-0265(99)00011-1)
984 0265(99)00011-1, 1999.
- 985 Manca, B., Burca, M., Giorgetti, A., Coatanoan, C., Garcia, M. J. and Iona, A.: Physical and biochemical
986 averaged vertical profiles in the Mediterranean regions: An important tool to trace the climatology of
987 water masses and to validate incoming data from operational oceanography, *J. Mar. Syst.*, 48(1–4), 83–
988 116, <https://doi.org/10.1016/j.jmarsys.2003.11.025>, 2004.
- 989 Míguez, B. M., Novellino, A., Vinci, M., Claus, S., Calewaert, J. B., Vallius, H., Schmitt, T., Pititto, A.,
990 Giorgetti, A., Askew, N., Iona, S., Schaap, D., Pinardi, N., Harpham, Q., Kater, B. J., Populus, J., She,
991 J., Palazov, A. V., McMeel, O., Oset, P., Lear, D., Manzella, G. M. R., Gorringe, P., Simoncelli, S.,
992 Larkin, K., Holdsworth, N., Arvanitidis, C. D., Jack, M. E. M., Chaves Montero, M. del M., Herman, P.
993 M. J. and Hernandez, F.: The European Marine Observation and Data Network (EMODnet): Visions
994 and roles of the gateway to marine data in Europe, *Front. Mar. Sci.*, 6(JUL), 1–24,
995 <https://doi.org/10.3389/fmars.2019.00313>, 2019.
- 996 Moon, J., Lee, K., Tanhua, T., Kress, N. and Kim, I.: Temporal nutrient dynamics in the Mediterranean
997 Sea in response to anthropogenic inputs, , 5243–5251,
998 <https://doi.org/10.1002/2016GL068788>.Received, 2016.
- 999 Moore, C. M., Mills, M. M., Arrigo, K. R., Berman-Frank, I., Bopp, L., Boyd, P. W., Galbraith, E. D.,
1000 Geider, R. J., Guieu, C., Jaccard, S. L., Jickells, T. D., La Roche, J., Lenton, T. M., Mahowald, N. M.,
1001 Marañón, E., Marinov, I., Moore, J. K., Nakatsuka, T., Oschlies, A., Saito, M. A., Thingstad, T. F.,
1002 Tsuda, A. and Ulloa, O.: Processes and patterns of oceanic nutrient limitation, *Nat. Geosci.*, 6(9), 701–
1003 710, <https://doi.org/10.1038/ngeo1765>, 2013.
- 1004 Murphy, A. H.: Skill Scores Based on the Mean Square Error and Their Relationships to the Correlation
1005 Coefficient, *Mon. Weather Rev.*, 116(12), 2417–2424, [https://doi.org/10.1175/1520-](https://doi.org/10.1175/1520-0493(1988)116<2417:SSBOTM>2.0.CO;2)
1006 0493(1988)116<2417:SSBOTM>2.0.CO;2, 1988.
- 1007 Ozer, T., Gertman, I., Kress, N., Silverman, J. and Herut, B.: Interannual thermohaline (1979–2014) and
1008 nutrient (2002–2014) dynamics in the Levantine surface and intermediate water masses, *SE*
1009 *Mediterranean Sea*, *Glob. Planet. Change*, <https://doi.org/10.1016/j.gloplacha.2016.04.001>, 2017.
- 1010 Picco, P.: ed. Climatological atlas of the western Mediterranean. Santa Teresa Centre for Energy and
1011 Environmental Research, 1990.
- 1012 Piñeiro, S., González-Pola, C., Fernández-Díaz, J. M. and Balbin, R.: Thermohaline Evolution of the
1013 Western Mediterranean Deep Waters Since 2005: Diffusive Stages and Interannual Renewal Injections,
1014 *J. Geophys. Res. Ocean.*, 124(12), 8747–8766, <https://doi.org/10.1029/2019JC015094>, 2019.
- 1015 Pondaven, P., Ruiz-Pino, D., Druon, J. N., Fravallo, C. and Tréguer, P.: Factors controlling silicon and
1016 nitrogen biogeochemical cycles in high nutrient, low chlorophyll systems (the Southern Ocean and the
1017 North Pacific): Comparison with a mesotrophic system (the North Atlantic), *Deep. Res. Part I Oceanogr.*
1018 *Res. Pap.*, 46(11), 1923–1968, [https://doi.org/10.1016/S0967-0637\(99\)00033-3](https://doi.org/10.1016/S0967-0637(99)00033-3), 1999.
- 1019 Pujo-Pay, M., Conan, P., Oriol, L., Cornet-Barthaux, V., Falco, C., Ghiglione, J. F., Goyet, C., Moutin,
1020 T. and Prieur, L.: Integrated survey of elemental stoichiometry (C, N, P) from the western to eastern
1021 Mediterranean Sea, *Biogeosciences*, 8(4), 883–899, <https://doi.org/10.5194/bg-8-883-2011>, 2011.
- 1022 Rahav, E., Herut, B., Stambler, N., Bar-Zeev, E., Mulholland, M. R. and Berman-Frank, I.: Uncoupling
1023 between dinitrogen fixation and primary productivity in the eastern Mediterranean Sea, *J. Geophys. Res.*
1024 *Biogeosciences*, 118(1), 195–202, <https://doi.org/10.1002/jgrg.20023>, 2013.
- 1025 Reale, M., Giorgi, F., Solidoro, C., Di Biagio, V., Di Sante, F., Mariotti, L., Farneti, R. and Sannino, G.:
1026 The Regional Earth System Model RegCM-ES: Evaluation of the Mediterranean climate and marine
1027 biogeochemistry., 2020.
- 1028 Reul, A., Rodríguez, V., Jiménez-Gómez, F., Blanco, J. M., Bautista, B., Sarhan, T., Guerrero, F., Ruíz,



- 1029 J. and García-Lafuente, J.: Variability in the spatio-temporal distribution and size-structure of
1030 phytoplankton across an upwelling area in the NW-Alboran Sea, (W-Mediterranean), *Cont. Shelf Res.*,
1031 25(5–6), 589–608, <https://doi.org/10.1016/j.csr.2004.09.016>, 2005.
- 1032 Ribera d’Alcalà, M.: Nutrient ratios and fluxes hint at overlooked processes in the Mediterranean Sea,
1033 *J. Geophys. Res.*, 108(C9), <https://doi.org/10.1029/2002jc001650>, 2003.
- 1034 Ribera d’Alcalà, M., Civitarese, G., Conversano, F. and Lavezza, R.: Nutrient ratios and fluxes hint at
1035 overlooked processes in the Mediterranean Sea, *J. Geophys. Res. Ocean.*,
1036 108(9), <https://doi.org/10.1029/2002jc001650>, 2003.
- 1037 Rixen, M., Beckers, J. M., Brankart, J. M. and Brasseur, P.: A numerically efficient data analysis method
1038 with error map generation, *Ocean Model.*, 2(1–2), 45–60, [https://doi.org/10.1016/s1463-5003\(00\)00009-3](https://doi.org/10.1016/s1463-5003(00)00009-3), 2000.
- 1040 Roether, W. and Schlitzer, R.: Eastern Mediterranean deep water renewal on the basis of
1041 chlorofluoromethane and tritium data, *Dyn. Atmos. Ocean.*, 15(3–5), 333–354,
1042 [https://doi.org/10.1016/0377-0265\(91\)90025-B](https://doi.org/10.1016/0377-0265(91)90025-B), 1991.
- 1043 Roether, W., Manca, Beniamino B. Klein, B., Bregant, D., Georgopoulos, D., Beitzel, V. and
1044 KovaEevic, Vedrana Luchetta, A.: Recent Changes in Eastern Mediterranean Deep Waters., 1996.
- 1045 Roether, W., Klein, B., Bruno, B., Theocharis, A. and Kioroglou, S.: Progress in Oceanography
1046 Transient Eastern Mediterranean deep waters in response to the massive dense-water output of the
1047 Aegean Sea in the 1990s, , 74, 540–571, <https://doi.org/10.1016/j.pocean.2007.03.001>, 2007.
- 1048 Roether, W., Klein, B. and Hainbucher, D.: The Eastern Mediterranean Transient: Evidence for Similar
1049 Events Previously?, *Mediterr. Sea Temporal Var. Spat. Patterns*, 9781118847(January), 75–
1050 83, <https://doi.org/10.1002/9781118847572.ch6>, 2014.
- 1051 Salgado-Hernanz, P. M., Racault, M. F., Font-Muñoz, J. S. and Basterretxea, G.: Trends in
1052 phytoplankton phenology in the Mediterranean Sea based on ocean-colour remote sensing, *Remote
1053 Sens. Environ.*, 221(October 2018), 50–64, <https://doi.org/10.1016/j.rse.2018.10.036>, 2019.
- 1054 Sarmiento, J. L. and Toggweiler, J. R.: A new model for the role of the oceans in determining
1055 atmospheric PCO₂, *Nature*, 308(5960), 621–624, <https://doi.org/10.1038/308621a0>, 1984.
- 1056 Schröder, K., Gasparini, G. P., Tangherlini, M. and Astraldi, M.: Deep and intermediate water in the
1057 western Mediterranean under the influence of the Eastern Mediterranean Transient, *Geophys. Res. Lett.*,
1058 33(21), 2–7, <https://doi.org/10.1029/2006GL027121>, 2006.
- 1059 Schroeder, K., Gasparini, G. P., Borghini, M., Cerrati, G. and Delfanti, R.: Biogeochemical tracers and
1060 fluxes in the Western Mediterranean Sea , spring 2005, *J. Mar. Syst.*, 80(1–2), 8–24,
1061 <https://doi.org/10.1016/j.jmarsys.2009.08.002>, 2010.
- 1062 Schroeder, K., Tanhua, T., Bryden, H., Alvarez, M., Chiggiato, J. and Aracri, S.: Mediterranean Sea
1063 Ship-based Hydrographic Investigations Program (Med-SHIP), *Oceanography*, 28(3), 12–15,
1064 <https://doi.org/10.5670/oceanog.2015.71>, 2015.
- 1065 Schroeder, K., Chiggiato, J., Bryden, H. L., Borghini, M. and Ismail, S. Ben: Abrupt climate shift in the
1066 Western Mediterranean Sea, *Nat. Publ. Gr.*, 1–7, <https://doi.org/10.1038/srep23009>, 2016.
- 1067 Schroeder, K., Chiggiato, J., Josey, S. A., Borghini, M., Aracri, S. and Sparnocchia, S.: Rapid response
1068 to climate change in a marginal sea, , (May), 1–7, <https://doi.org/10.1038/s41598-017-04455-5>, 2017.
- 1069 Schroeder, K., Cozzi, S., Belgacem, M., Borghini, M., Cantoni, C., Durante, S., Petrizzo, A., Poiana, A.
1070 and Chiggiato, J.: Along-Path Evolution of Biogeochemical and Carbonate System Properties in the
1071 Intermediate Water of the Western Mediterranean, *Front. Mar. Sci.*, 7(May), 1–19,
1072 <https://doi.org/10.3389/fmars.2020.00375>, 2020.
- 1073 SeaDataNet Group: Data Quality Control Procedures, Tech. Rep. Version 2.0, SeaDataNet consortium,

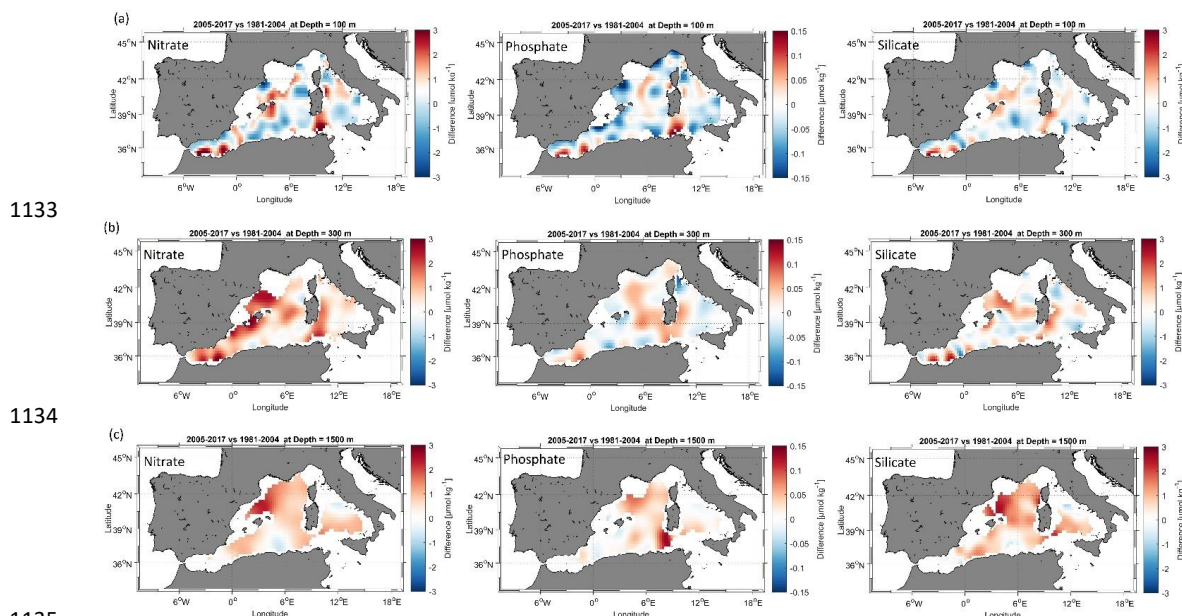


- 1074 available at: [https://www.seadatanet.org/content/download/596/3118/file/](https://www.seadatanet.org/content/download/596/3118/file/SeaDataNet_QC_procedures_V2_(May_2010).pdf?version=1)
1075 [SeaDataNet_QC_procedures_V2_\(May_2010\).pdf?version=1](https://www.seadatanet.org/content/download/596/3118/file/SeaDataNet_QC_procedures_V2_(May_2010).pdf?version=1), 2010. Shepherd, J. G., Brewer, P. G.,
1076 Oschlies, A. and Watson, A. J.: Ocean ventilation and deoxygenation in a warming world: posters,
1077 *Philos. Trans. R. Soc. A Math. Phys. Eng. Sci.*, 375(2102), 20170241,
1078 <https://doi.org/10.1098/rsta.2017.0241>, 2017.
- 1079 Simoncelli, S., Tonani, M., Grandi, A., Coatanoan, C., Myroshnychenko, V., Sagen, H., Back, O., Scory,
1080 S., Schlitzer, R., and Fichaut, M.: First Release of the SeaDataNet Aggregated Data Sets Products, WP10
1081 Second Year Report – DELIVERABLE D10.2, <https://doi.org/10.13155/49827>, 2014.
- 1082 Simoncelli, S., Coatanoan, C., Myroshnychenko, V., Sagen, H., Bäck, O., Scory, S., Grandi, A., Barth,
1083 A., and Fichaut, M.: SeaDataNet. First Release of Regional Climatologies. WP10 Third Year Report -
1084 DELIVERABLE D10.3., Tech. rep., SeaDataNet, 20 <https://doi.org/10.13155/50381>, 2015.
- 1085 Simoncelli, S., Grandi, A., and Iona, S.: New Mediterranean Sea climatologies. *Bollettino di*
1086 *Geofisica*, 57, 2016. Sospedra, J., Niencheski, L. F. H., Falco, S., Andrade, C. F. F., Attisano, K. K. and
1087 Rodilla, M.: ScienceDirect Identifying the main sources of silicate in coastal waters of the Southern Gulf
1088 of Valencia (Western Mediterranean Sea), *Oceanologia*, 60(1), 52–
1089 64, <https://doi.org/10.1016/j.oceano.2017.07.004>, 2018.
- 1090 Stöven, T. and Tanhua, T.: Ventilation of the mediterranean sea constrained by multiple transient tracer
1091 measurements, *Ocean Sci.*, 10(3), 439–457, <https://doi.org/10.5194/os-10-439-2014>, 2014.
- 1092 Tanhua, T., Hainbucher, D., Schroeder, K., Cardin, V., Álvarez, M. and Civitarese, G.: The
1093 Mediterranean Sea system: A review and an introduction to the special issue, *Ocean Sci.*, 9(5), 789–
1094 803, <https://doi.org/10.5194/os-9-789-2013>, 2013.
- 1095 Teruzzi, A., Bolzon, G., Cossarini, G., Lazzari, P., Salon, S., Crise, A., and Solidoro, C.: Mediterranean
1096 Sea Biogeochemical Reanalysis (CMEMS MED-Biogeochemistry) [Data set]. Copernicus Monitoring
1097 Environment Marine Service (CMEMS).
1098 https://doi.org/10.25423/MEDSEA_REANALYSIS_BIO_006_008, 2019.
- 1099 Testor, P., Bosse, A., Houpert, L., Margirier, F., Mortier, L., Legoff, H., Dausse, D., Labaste, M.,
1100 Karstensen, J., Hayes, D., Olita, A., Ribotti, A., Schroeder, K., Chiggiato, J., Onken, R., Heslop, E.,
1101 Mourre, B., D’ortenzio, F., Mayot, N., Lavigne, H., de Fommervault, O., Coppola, L., Prieur, L.,
1102 Taillandier, V., Durrieu de Madron, X., Bourrin, F., Many, G., Damien, P., Estournel, C., Marsaleix, P.,
1103 Taupier-Letage, I., Raimbault, P., Waldman, R., Bouin, M. N., Giordani, H., Caniaux, G., Somot, S.,
1104 Ducrocq, V. and Conan, P.: Multiscale Observations of Deep Convection in the Northwestern
1105 Mediterranean Sea During Winter 2012–2013 Using Multiple Platforms, *J. Geophys. Res. Ocean.*,
1106 123(3), 1745–1776, <https://doi.org/10.1002/2016JC012671>, 2018.
- 1107 Theocharis, A., Lascaratos, A., & Sofianos, S.: Variability of sea water properties in the Ionian, Cretan
1108 and Levantine seas during the last century. In *Tracking Long-Term Hydrological Change in the*
1109 *Mediterranean Sea*, CIESM Workshop Series (Vol. 16, pp. 71-78), 2002.
- 1110 Troupin, C., MacHín, F., Ouberdous, M., Sirjacobs, D., Barth, A. and Beckers, J. M.: High-resolution
1111 climatology of the northeast Atlantic using Data-Interpolating Variational Analysis (Diva), *J. Geophys.*
1112 *Res. Ocean.*, 115(8), 1–20, <https://doi.org/10.1029/2009JC005512>, 2010.
- 1113 Troupin, C., Barth, A., Sirjacobs, D., Ouberdous, M., Brankart, J. M., Brasseur, P., Rixen, M., Alvera-
1114 Azcárate, A., Belounis, M., Capet, A., Lenartz, F., Toussaint, M. E. and Beckers, J. M.: Generation of
1115 analysis and consistent error fields using the Data Interpolating Variational Analysis (DIVA), *Ocean*
1116 *Model.*, 52–53, 90–101, <https://doi.org/10.1016/j.ocemod.2012.05.002>, 2012.
- 1117 Troupin, C., Watelet, S., Ouberdous, M., Sirjacobs, D., Barth, A., Toussaint, M. and Beckers, J.: Data
1118 Interpolating Variational Analysis User Guide, , 836723, <https://doi.org/10.5281/zenodo.836723>, 2018.
- 1119 Van Cappellen, P., Powley, H. R., Emeis, K. C. and Krom, M. D.: A biogeochemical model for
1120 phosphorus and nitrogen cycling in the Eastern Mediterranean Sea: Part 1: Model development,
1121 initialization and sensitivity, *J. Mar. Syst.*, 139, 460–471, <https://doi.org/10.1016/j.jmarsys.2014.08.016>,



- 1122 2014.
- 1123 Vargas-yáñez, M.: Updating temperature and salinity mean values and trends in the Western
1124 Mediterranean : The RADMED project Progress in Oceanography Updating temperature and salinity
1125 mean values and trends in the Western Mediterranean : The RADMED project, Prog. Oceanogr.,
1126 157(September), 27–46, <https://doi.org/10.1016/j.pocean.2017.09.004>, 2017.
- 1127 Weatherall, P., Marks, K. M., Jakobsson, M., Schmitt, T., Tani, S., Arndt, J. E., Rovere, M., Chayes, D.,
1128 Ferrini, V. and Wigley, R.: A new digital bathymetric model of the world’s oceans, Earth Sp. Sci., 2,
1129 331–345, <https://doi.org/10.1002/2015EA000107>, 2015.
- 1130 Williams, R. G. and Follows, M. J.: Physical Transport of Nutrients and the Maintenance of Biological
1131 Production, in Ocean Biogeochemistry, pp. 19–51., 2003.

1132 Appendix



1135 **Figure A1.** (a) Difference field at 100 m between the 1981-2004 climatology and the 2005-2017
1136 climatologies; (b) Difference field at 300 m (c) Difference field at 1500.

1138